Materials Today Physics

Two-Dimensional WSe2/SnSe p-n Junctions Secure Ultrahigh Thermoelectric Performance in n-type Pb/I Co-doped Polycrystalline SnSe

--Manuscript Draft--

Manuscript Number:	MTP-D-20-00399R1
Article Type:	Research Paper
Keywords:	thermoelectric; SnSe; n-type; p-n junction; doping
Corresponding Author:	Zhi-Gang Chen University of Southern Queensland AUSTRALIA
First Author:	Yue-Xing Chen
Order of Authors:	Yue-Xing Chen
	Xiao-Lei Shi
	Zhuang-Hao Zheng
	Fu Li
	Wei-Di Liu
	Wen-Yi Chen
	Xin-Ru Li
	Guang-Xing Liang
	Jing-Ting Luo
	Ping Fan
	Zhi-Gang Chen
Abstract:	In this study, we, for the first time, introduce p-type two-dimensional (2D) WSe2 nanoinclusions in n-type Pb/I co-doped SnSe matrix to form WSe2/SnSe p-n junctions. These p-n junctions act as energy barriers and effective phonon scattering sources, leading to a high figure-of-merit (ZT) of ~1.35 at ~790 K in n-type polycrystalline SnSe. First-principles density functional theory calculation results indicates that I-doping shifts Fermi level up into conduction bands of SnSe, making the system n-type behavior, while both Pb and I dopants act as point-defect-based short-wavelength phonon scattering centers. The introduced p-type 2D WSe2 nanoinclusions induce high-density WSe2/SnSe interfaces that act as p-n junctions, which block the electron carriers and rationally tune the carrier density, contributing to a high absolute Seebeck coefficient of ~470.7 μV K-1 and a high power factor of ~5.9 μW cm-1 K-2 . Meanwhile, the dense phase boundaries and considerable lattice strains by the introduced 2D WSe2 nanoinclusions significantly strengthen the mid- and long-wavelength phonon scattering, giving rise to a much low thermal conductivity of 0.35 W m-1 K-1 and in turn a high ZT of ~1.35. This study provides a new strategy to achieve high thermoelectric performance in n-type polycrystalline SnSe.
Suggested Reviewers:	Li-Dong Zhao Beihang University zhaolidong@buaa.edu.cn Expert in SnSe-based thermoelectrics.
	Xiaolin Wang University of Wollongong xiaolin_wang@uow.edu.au Expert in SnSe-based thermoelectrics.
Opposed Reviewers:	
Response to Reviewers:	The response to specific reviewer and editor comments has been uploaded by a single Word file in the system.

Cover Letter

CENTRE FOR FUTURE MATERIALS
Prof. Dr. Zhi-Gang Chen
Professor (Energy Materials)
PHONE +61 74631336; +61 423324518 | FAX +61 746312110
EMAIL zhigang.chen@usq.edu.au

UNIVERSITY
OF SOUTHERN
QUEENSLAND

12th, October 2020

Dear editors,

With this letter, I am submitting a revised manuscript entitled "**Two-Dimensional WSe$_2$/SnSe *p-n* Junctions Secure Ultrahigh Thermoelectric Performance in *n*-type Pb/I Co-doped Polycrystalline SnSe**" for your assessment for publication in ***Materials Today Physics***. I certify that this is an original manuscript that has not been submitted elsewhere for publication.

We have carefully revised the manuscript according to your and reviewers' comments. The revised parts have been marked as red color in the manuscript, and the responses to the reviewers have also been submitted as a single word file. Besides, we also checked and revised the minor mistakes in references.

Thank you for your time with this submission and I look forward to hearing good news from you.

Zhigang Chen

University of Southern Queensland

Response to reviewers

Reviewer #1:

In the manuscript "Two-Dimensional WSe_2*/SnSe p-n Junctions Secure Ultrahigh Thermoelectric Performance in n-type Pb/I Co-doped Polycrystalline SnSe", the authors focus on improving thermoelectric properties of n-type polycrystalline SnSe by Pb/I co-doped and introducing* WSe_2 *nanoinclusions. With step by step optimizing process, the maximum ZT of 1.35 is achieved at 790 K. The authors introduced the* WSe_2 *nanoinclusions into the SnSe matrix led to the enhancement of electrical and thermal transport properties simultaneously, confirming its positive effects on SnSe. The manuscript is well constructed, and the results are meaningful and interesting. Therefore, I would like to recommend this manuscript to be published by Materials Today Physics after minor revision. The comments are given as following.*

Comment 1. After introducing WSe_2 *phase, the carrier density decreased with increasing* WSe_2*, the authors should give more explanations. (Figure 6d).*

Response： We appreciate Reviewer #1 for his/her time in reviewing our manuscript. In **Figure 6(d)**, we present the variation of n for $Sn_{0.97}Pb_{0.03}Se_{0.89}I_{0.06}$-$y$ % WSe_2 as a function of y value. The introduction of p-type 2D WSe_2 nanoinclusions induces high-density WSe_2/SnSe interfaces that act as p-n junctions, which arises the “depletion layer effect” and leads to the decrease of n. We have added these explanations on **Page 18** of the revised manuscript. In addition, **Figure 6(f)** illustrates the mechanism of depletion layer effect by WSe_2/SnSe phase boundaries that act as p-n junctions. On the other hand, the high-density WSe_2/SnSe interfaces significantly filter the electron carriers which will also contribute to the decrease of n. The decline of n is further confirmed by the enhancement of absolute S (**Figure 6(a)**) and reduction of effective mass m^* (**Figure 6(e)**).

Comment 2 Page 9, line 14; page 10, line 3; and page 13, line 8, there are editing problems refer to the measuring directions.

Response： We have solved the editing problems in the revised manuscript.

Comment 3 The density ρ was measured using the Archimedes method, but the authors did not give the values for the samples.

Response: We have added **Table S1** which lists the densities of as the fabricated samples in Supporting Information.

Table R1 (**Table S1** in supporting information). Measured densities of samples. The theoretical density of pure SnSe is 6.179 g cm^{-3}.

Sample (Nominal composition)	**Measured density (g cm^{-3})**	**Relative density (%)**
$SnSe_{0.95}$	6.08	98.4%
$Sn_{0.99}Pb_{0.01}Se_{0.93}I_{0.02}$	6.03	97.6%
$Sn_{0.97}Pb_{0.03}Se_{0.89}I_{0.06}$	6.02	97.4%
$Sn_{0.95}Pb_{0.05}Se_{0.85}I_{0.10}$	6.01	97.2%
$Sn_{0.97}Pb_{0.03}Se_{0.89}I_{0.06}$-0.5 % WSe_2	6.02	97.4%
$Sn_{0.97}Pb_{0.03}Se_{0.89}I_{0.06}$-1.0 % WSe_2	6.10	98.7%
$Sn_{0.97}Pb_{0.03}Se_{0.89}I_{0.06}$-2.0 % WSe_2	6.10	98.7%

Comment 4 How to determine the error bars in the measured data? This information should be given in the experimental part.

Response: We have added the related content in the revised manuscript as: “In terms of the determination of error bars, the combined uncertainty for the experimental determination of *ZT* is about 15%–20% and is caused by the five respective measurement including *σ*, *S*, *D*, and *ρ*.” on **Page 6**.

Reviewer #2

The authors introduce the two-dimensional WSe_2/SnSe p-n junctions to secure ultrahigh thermoelectric performance in n-type Pb/I co-doped polycrystalline SnSe. Because pristine polycrystalline SnSe possess a relatively low $S^2\sigma$ and high κ, many strategies have been employed to improve their thermoelectric performance, especially for the n-type polycrystalline SnSe. After carefully going through this manuscript, I found this work is high-quality with very clear logic and comprehensive characterizations and calculations. The results are interesting and promising, to my knowledge, a ZT of 1.35 in n-type poly-SnSe is rarely reported (the authors also list the comparison in Table 2), therefore this work should gain significant attention. In addition, the discussions are comprehensive, and many results can be well supported by the direct evidence in either main text or in the supporting file. Therefore, I recommend this work be published in this journal after some minor revisions listed below:

Comment 1: The measured densities ρ should be given in the experimental part since it is an important part to compose the thermal conductivity κ. Generally, either relative mass density (%) or actual mass density values (g cm^{-3}) are acceptable.

Response: Thank you for your constructive suggestion. We have added **Table S1** which lists the densities of as the fabricated samples in Supporting Information.

Table R1 (**Table S1** in supporting information). Measured densities of samples. The theoretical density of pure SnSe is 6.179 g cm^{-3}.

Sample (Nominal composition)	**Measured density (g cm^{-3})**	**Relative density (%)**
$SnSe_{0.95}$	6.08	98.4%
$Sn_{0.99}Pb_{0.01}Se_{0.93}I_{0.02}$	6.03	97.6%
$Sn_{0.97}Pb_{0.03}Se_{0.89}I_{0.06}$	6.02	97.4%
$Sn_{0.95}Pb_{0.05}Se_{0.85}I_{0.10}$	6.01	97.2%
$Sn_{0.97}Pb_{0.03}Se_{0.89}I_{0.06}$-0.5 % WSe_2	6.02	97.4%

$Sn_{0.97}Pb_{0.03}Se_{0.89}I_{0.06}$-1.0 % WSe_2	6.10	98.7%
$Sn_{0.97}Pb_{0.03}Se_{0.89}I_{0.06}$-2.0 % WSe_2	6.10	98.7%

Comment 2: Why the authors choose to sinter the pellets at 773 K, which is below the temperature of SnSe phase transition of 800 K?

Response: The sintered SnSe samples at 773 K by SPS possess a relatively density higher than 95 % as described in **Table R1** (**Table S1** of supporting information). The sintered temperature is lower than the phase transition of ~800 K, which can significantly improve the stability of the as-sintered pellets.

Comment 3: Fig 7b should add error bars since it is also the important data achieved from the measured thermal conductivity κ.

Response: In the revised manuscript, we have added the error bars in Figure R1 (**Figure 7b)**.

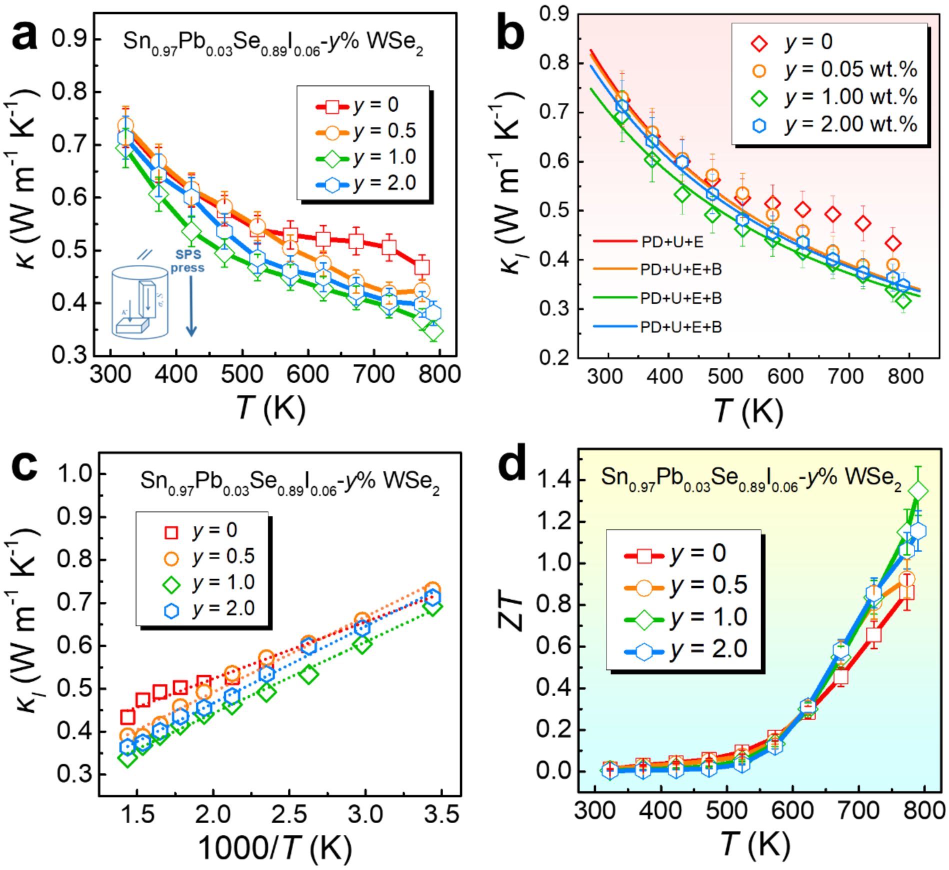

Figure R1 (**Figure 7** in the revised manuscript). *T*-dependent (a) κ and (b) κ_l of $Sn_{0.97}Pb_{0.03}Se_{0.89}I_{0.06}$-*y* % WSe_2. The calculated κ_l using Callaway model are included in (b), including impurity/point defect phonon scattering τ_{im}^{-1} (PD), phonon-phonon Umklapp scattering τ_U^{-1} (U), phase boundary phonon scattering τ_{pb}^{-1} (PB) and electron-phonon scattering τ_{ep}^{-1} (E). (c) 1000/*T*-dependent κ_l of $Sn_{0.97}Pb_{0.03}Se_{0.89}I_{0.06}$-*y* % WSe_2. (d) *T*-dependent *ZT* of $Sn_{0.97}Pb_{0.03}Se_{0.89}I_{0.06}$-*y* % WSe_2. Here *y* is 0, 0.5, 1.0, and 2.0, respectively. All the properties are measured or determined along the // direction.

Comment 4: The information of some references should be updated, such as [18] and [20].

Response: We had updated the references of [18] and [20] in the revised manuscript:

[18] X.-L. Shi, W.-Y. Chen, X. Tao, J. Zou, and Z.-G. Chen, Mater. Horiz. (2020). DOI: 10.1039/D0MH00954G.

[21] X.-L. Shi, W.-D. Liu, A.-Y. Wu, V.T. Nguyen, H. Gao, Q. Sun, R. Moshwan, J. Zou, and Z.-G. Chen, InfoMat 2 (2020) 1201-1215.

Two-Dimensional WSe_2/SnSe p-n Junctions Secure Ultrahigh Thermoelectric Performance in n-type Pb/I Co-doped Polycrystalline SnSe

Yue-Xing Chen [1,†], *Xiao-Lei Shi* [2,3,†], *Zhuang-Hao Zheng* [1,†,*], *Fu Li* [1], *Wei-Di Liu* [3], *Wen-Yi Chen* [3], *Xin-Ru Li* [1], *Guang-Xing Liang* [1], *Jing-Ting Luo* [1], *Ping Fan* [1,*], *Zhi-Gang Chen* [2,3,*]

[1] Shenzhen Key Laboratory of Advanced Thin Films and Applications, Key Laboratory of Optoelectronic Devices and Systems of Ministry of Education and Guangdong Province, College of Physics and Optoelectronic Engineering, Shenzhen University, Shenzhen 518060, P. R. China;

[2] Centre for Future Materials, University of Southern Queensland, Springfield Central, Brisbane, Queensland 4300, Australia;

[3] School of Mechanical and Mining Engineering, The University of Queensland, St Lucia, Brisbane, Queensland 4072, Australia.

[†] These authors contribute equally to this work.

* Corresponding authors:

Zhuang-Hao Zheng: zhengzh@szu.edu.cn;

Ping Fan: fangp@szu.edu.cn;

Zhi-Gang Chen: zhigang.chen@usq.edu.au, zhigang.chen@uq.edu.au.

Abstract:

In this study, we, for the first time, introduce p-type two-dimensional (2D) WSe_2 nanoinclusions in n-type Pb/I co-doped SnSe matrix to form WSe_2/SnSe p-n junctions. These p-n junctions act as energy barriers and effective phonon scattering sources, leading to a high figure-of-merit (*ZT*) of ~1.35 at ~790 K in n-type polycrystalline SnSe. First-principles density functional theory calculation results indicates that I-doping shifts Fermi level up into conduction bands of SnSe, making the system n-type behavior, while both Pb and I dopants act as point-defect-based short-wavelength phonon scattering centers. The introduced p-type 2D WSe_2 nanoinclusions induce high-density WSe_2/SnSe interfaces that act as p-n junctions, which block the electron carriers and rationally tune the carrier density, contributing to a high absolute Seebeck coefficient of ~470.7 $\mu V K^{-1}$ and a high power factor of ~5.9 $\mu W cm^{-1} K^{-2}$. Meanwhile, the dense phase boundaries and considerable lattice strains by the introduced 2D WSe_2 nanoinclusions significantly strengthen the mid- and long-wavelength phonon scattering, giving rise to a much low thermal conductivity of 0.35 $W m^{-1} K^{-1}$ and in turn a high *ZT* of ~1.35. This study provides a new strategy to achieve high thermoelectric performance in n-type polycrystalline SnSe.

Keywords: thermoelectric; SnSe; n-type; p-n junction; doping.

1. Introduction

Owing to the capability for direct energy conversion between heat and electricity, thermoelectric materials have been attracted significant attentions with full potentials for solving the issues of fossil fuel depletion and environmental pollutions by waste-heat recovery [1, 2]. The energy conversion efficiency of thermoelectric materials is evaluated by the dimensionless figure-of-merit ZT, defined as $ZT = S^2\sigma T/\kappa = S^2\sigma T/(\kappa_e + \kappa_l)$ [3], where σ is the electric conductivity, S is the Seebeck coefficient, $S^2\sigma$ is the power factor, T is the absolute temperature, κ is the total thermal conductivity, κ_e is the electronic thermal conductivity, and κ_l is the lattice thermal conductivity. In general, a high $S^2\sigma$ and a low κ are both required to achieve a high ZT value [4, 5]. To date, many thermoelectric materials have exhibited excellent thermoelectric performance with ZT values >2 by rational thermoelectric designs, such as $AgSbTe_2$ (ZT = ~2.1 at 573 K by Se-doping) [6], PbTe (ZT = ~2.51 at 823 K by doping with Na, Eu, and Sn) [7], GeTe (ZT = ~2.4 at 600 K by doping with Pb and Bi) [8], liquid-like $Cu_{2-x}Se$ (ZT = ~2.62 at 1029 K by 2 % Al-doping) [9, 10], and SnSe crystals (ZT = ~2.8 at 773 K by Br-doping) [11].

Among these state-of-the-art thermoelectric materials, SnSe-based bulk materials have drawn considerable attention due to their suitable bandgap (~0.9 eV) [3], cost-effectiveness [12], and low-toxic feature [13], making them good candidates with great potentials for applications in low-cost thermoelectric devices [14, 15]. Especially, n-type SnSe single crystals were reported to exhibit a record-high ZT of ~2.8 at 773 K [11], owing to their high $S^2\sigma$ and remarkably low κ. However, the undesirable mechanical properties make the single crystals easy to cleave along the *b*- or *c*-directions [12], and the issues of high-cost and time-consuming in the production of SnSe single crystals severely limit their applications in thermoelectric devices at an industrial scale [11, 12, 16]. Therefore, mechanically robust and low-cost polycrystalline SnSe becomes a promising alternative candidate, and has gained significant attention in recent years.

Because pristine polycrystalline SnSe possess a relatively low $S^2\sigma$ and high κ [17], many strategies have been employed to improve their thermoelectric performance [18], such as vacancy engineering [19-21], doping [22-25], multi-phase alloying [26-28], anisotropy strengthening [29, 30], and nanoporosity design [31, 32]. The peak ZT values have been improved from ~0.5 to ~2.5 for p-type polycrystalline SnSe [3, 18, 33, 34]. However, it is still challenging with only few works to achieve a high ZT of >1.0 in the n-type polycrystalline SnSe due to the p-type nature of pristine SnSe [35-40], and the mechanisms for the n-type thermoelectric behaviors in SnSe are still unclear. Moreover, developing high-performance n-type SnSe-based polycrystalline is urgent because same material systems are the best for the assembly of thermoelectric devices due to their similar thermodynamics, mechanical and welding properties.

I^- can release extra electrons into the system when substituting Se-sites (Se^{2-}) in SnSe, realizing n-type doping. By controlling the I-doping level, a well-tuned electron concentration can be achieved to optimize $S^2\sigma$. In addition, because Pb^{2+} possesses a much larger ionic radius of 1.20 Å than Sn^{2+} (0.93 Å) while I^- also possesses a larger ionic radius of 2.16 Å than Se^{2-} (1.84 Å), both Pb and I can act as point-defect-based phonon scattering centers to reduce κ (κ_l) by strengthening the short-wavelength phonon scattering. Based on Pb/I co-doping, to further realize high $S^2\sigma$ and low κ_l, one of the most effective strategies is introducing suitable nanoinclusions in the SnSe matrix [3]. The nanoinclusions should possess low dimensions to provide more phase boundaries as energy barriers to filter or block carriers and in turn improve S, and act as phonon scattering sources to strengthen the phonon scattering and in turn reduce κ_l. To realize this objective, we found p-type two-dimensional (2D) WSe_2 nanoinclusions are good candidates. WSe_2 possesses a high melting point of >1473 K [41], which is much higher than that of SnSe (1134 K) [3], therefore WSe_2 can be well maintained in SnSe matrix. WSe_2 is a typical p-type semiconductor that possesses a typical bandgap of ~1.5 eV and a unique 2D crystal structure [42], which can form high-density WSe_2-SnSe interfaces with the n-type SnSe phase, acting as p-n junctions. Such a strong energy barrier can block the electron carriers and rationally tune the carrier density, contribute to a high S. Besides, 2D WSe_2 was pointed out to has an ultralow intrinsic κ of only 0.05 W m^{-1} K^{-1} [41]. In addition, the introducing of 2D WSe_2 nanoinclusions provides extra phonon scattering sources in the polycrystals, including the high-density phase boundaries that target to scatter the long-wavelength phonons, and significant strain fields in the surrounding SnSe lattices. Therefore, we combine Pb/I co-doping that enable an n-type thermoelectric behavior and introduce 2D WSe_2 nanoinclusions to achieve high-performance n-type polycrystalline SnSe, as illustrated in **Figure 1(a)**.

2. Experimental Details

Fabrication. n-type polycrystalline SnSe pellets were fabricated by a combination of solid-state reaction and sparkle plasma sintering (SPS) technique. High-purity Sn chunk (99.99 %), Se chunk (99.99 %), PbI_2 powders (99.99 %), and WSe_2 nanopowders (99.9 %) were weighed as precursors, in which PbI_2 acted as dopant sources, and WSe_2 nanopowders acted as nanoinclusions. To reduce the native Sn vacancy concentration in pristine SnSe for promoting the n-type doping, the ratio of Se to Sn was set as 0.95:1, described as $SnSe_{0.95}$ (nominal composition). Two sets of compositions, namely $Sn_{1-x}Se_{0.95-2x}(PbI_2)_x$ (x = 0, 0.01, 0.03, and 0.05) and $Sn_{0.97}Pb_{0.03}Se_{0.89}I_{0.06}$-$y$ % WSe_2 (y = 0.5, 1.0, 2.0, and 4.0), were determined. The mixed precursors were loaded and sealed into evacuated quartz tubes with a pressure of $<10^{-4}$ Pa, and carefully sealed. The quartz tubes were placed in a box furnace and heated up to 1223 K with a heating rate of 100 K h^{-1}, soaking for 24 h. The tubes were slowly cooling down and broken. The obtained ingots were ground into powders by mortar-pestle and consolidated by using a SPS system (LABOX-325, Japan) at 773 K for 5 min under the pressure of 50 MPa. The sintered pellets were cylindric with dimensions of Φ10 mm × 12 mm, as shown in **Figure 1(b)** (top).

Characterization. For our fabricated n-type polycrystalline SnSe, the phases were confirmed by X-ray diffraction (XRD, CuKα, Riguku, Japan), the morphologies were investigated by field emission scanning electron microscopy (FE-SEM, Zeiss Merlin, Germany), the nanostructures were studied by spherical aberration-corrected (Cs-corrected) scanning transmission electron microscopy (STEM, Titan Cubed Themis G2 300, FEI, USA), and the real compositions were determined by electron probe micro-analyzer (EPMA, JXA8230, JEOL) and energy dispersive spectrometer (EDS) embedded in the FE-SEM and Cs-corrected STEM.

Performance. Polycrystalline SnSe is a typical anisotropy material due to its 2D orthorhombic crystal structure with strong anharmonic bonding [43, 44]. To evaluate the thermoelectric performance of our fabricated n-type polycrystalline SnSe, the pellets were cut into small pieces to measure the properties along the direction perpendicular (abbreviated as ⊥) and parallel (abbreviated as //) to the sintering pressure, as illustrated in **Figure 1(b)** (bottom). S and σ were measured from 300 to 790 K using an Ulvac-Riko ZEM-3 instrument in a thin helium atmosphere. κ was calculated using the relationship of $\kappa = D\rho C_p$ [19], in which the density ρ was measured using the Archimedes method [19], as shown in **Table S1**, and thermal diffusivity D was measured using laser flash equipment (NETZSCH Laser Flash Apparatus LFA 457, Germany). Specific heat C_p were taken from the literature [11]. The carrier concentrations n were derived from the formula $n = 1/eR_{\mathrm{H}}$, where e is the electronic charge, and R_{H} is the Hall coefficient. R_{H} was measured by the Van der Pauw method using a Hall measurement system (Lake Shore 8400 Series, Model 8404, USA) under a reversible magnetic field (0.8 T) in a wide temperature range from 300 to 773 K. The carrier mobility μ was calculated by $\mu = \sigma R_{\mathrm{H}}$. In terms of the determination of error bars, the combined uncertainty for the experimental determination of ZT is about 15%–20% and is caused by the five respective measurement including σ, S, D, and ρ.

Calculation. The calculations in this work were based on first-principles density functional theory (DFT). The structural relaxations and electronic structures were carried out using the projector augmented wave (PAW) method as implemented in the VASP code [45], and the exchange-correlation functional was approximated using the generalized gradient approximation (GGA) [46] with Perdew-Burke-Ernzerhof (PBE) parametrization [47]. The cut-off energy of the plane-wave was set to be 500 eV to ensure convergence. The convergence criteria of the force and the energy were 1×10^{-3} eV Å^{-1} and 1×10^{-7} eV, respectively. The 2D Brillouin zone integration was done with a ***k***-mesh density of 100/*a* [48]. The doping SnSe systems were constructed by a 2 × 2 ×2 (64 atoms) supercell.

3. Results and Discussions

In order to optimize the thermoelectric performance of our n-type polycrystalline SnSe pellets, the best concentrations of Pb, I, and 2D WSe_2 nanoinclusions are firstly explored. Two sets of compositions, namely $Sn_{1-x}Pb_xSe_{0.95-2x}I_{2x}$ (x = 0, 0.01, 0.03, and 0.05) and $Sn_{0.97}Pb_{0.03}Se_{0.89}I_{0.06}$-$y$ % WSe_2 (y = 0.5, 1.0, 2.0, and 4.0), were determined. **Figure 1(c)** compares the temperature-dependent *ZT* of our fabricated n-type polycrystalline SnSe pellets doped with different content of Pb, I, and 2D WSe_2 nanoinclusions, in which a promising *ZT* of ~0.9 at 773 K can be achieved by co-doping with 3 % Pb and 6 % I (x = 0.03), and a high *ZT* of ~1.35 at 790 K can be further achieved by introducing 1 % 2D WSe_2 nanoinclusion (y = 1.0). Such an outstanding thermoelectric performance possesses full potentials for applying in thermoelectric devices as n-type “legs” for the high-temperature power generation.

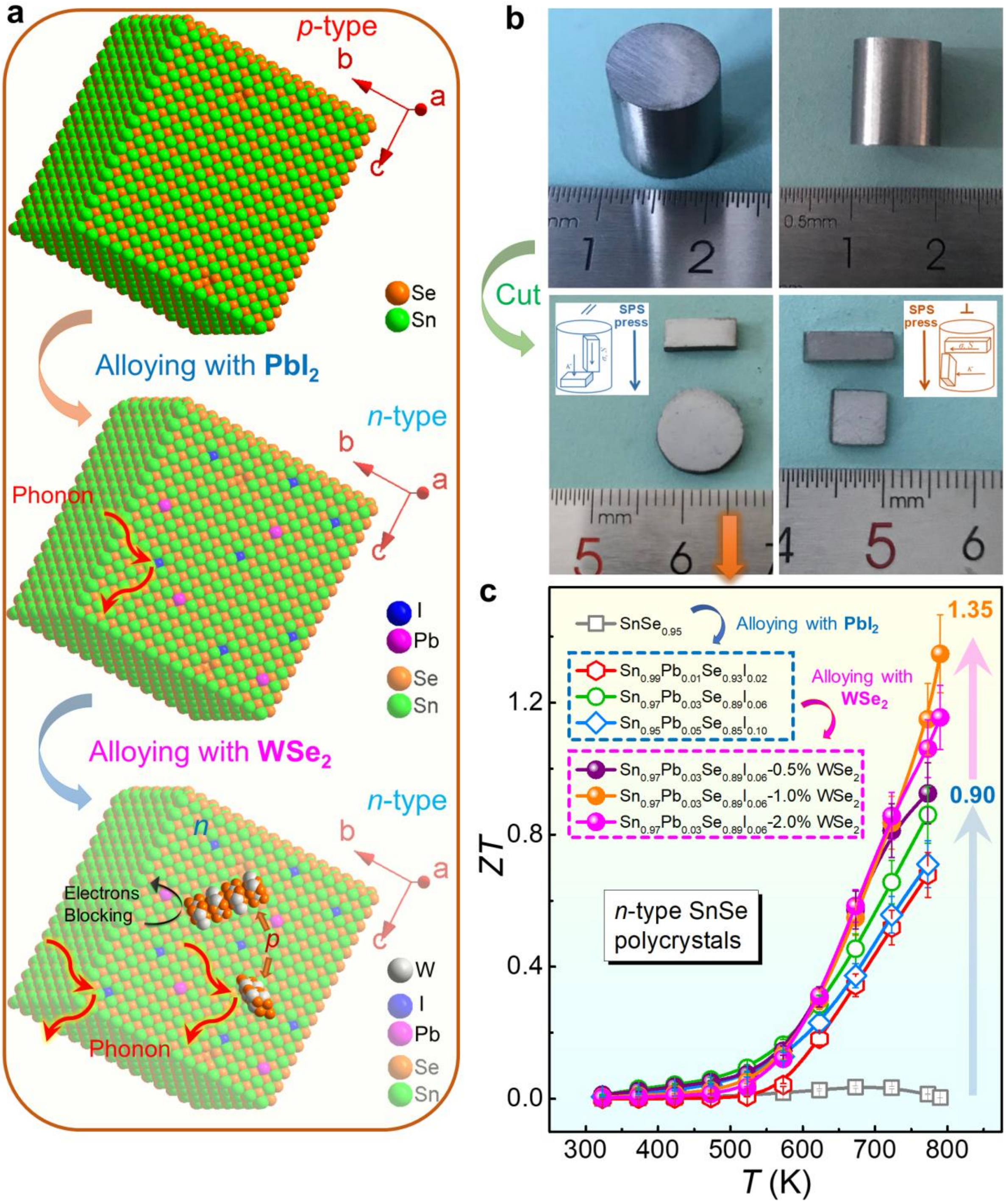

Figure 1. (a) Schematic diagrams of the strategies for boosting the thermoelectric performance of n-type polycrystalline SnSe, including Pb/I co-doping and alloying with WSe_2 nanoinclusions. (b) Optical images of the n-type polycrystalline SnSe pellets doped with 3 % Pb and 6 % I and alloyed with 1 % WSe_2 nanoinclusions (top). The bulk samples are cut for evaluating their thermoelectric performance along the direction parallel (//, bottom-left) and perpendicular (⊥, bottom-right) to the sintering pressure. (c) Temperature-dependent *ZT* of n-

type polycrystalline SnSe pellets doped with different content of Pb, I, and WSe_2 nanoinclusions.

Because the real compositions may be slightly different from the nominal compositions during the solid-state reaction and SPS processing, we determined the real compositions of our fabricated $Sn_{1-x}Pb_xSe_{0.95-2x}I_{2x}$ pellets by using EPMA, and the results are listed in **Table 1**. As can be seen, the solubility of I should be ~0.5 % since the real I contents for $x = 0.03$ and 0.05 are almost the same, while the Pb has not reached its upper limit of solubility in SnSe.

Table 1. Comparison of nominal and real compositions of the as-fabricated $Sn_{1-x}Pb_xSe_{0.95-2x}I_{2x}$ bulk samples.

x **value**	**Nominal composition**	**Real composition**	**Sn (at%)**	**Se (at%)**	**Pb (at%)**	**I (at%)**
0	$SnSe_{0.95}$	SnSe	50.01	49.99	0	0
0.01	$Sn_{0.99}Pb_{0.01}Se_{0.93}I_{0.02}$	$Sn_{0.989}Pb_{0.011}Se_{0.962}I_{0.001}$	50.37	48.99	0.56	0.08
0.03	$Sn_{0.97}Pb_{0.03}Se_{0.89}I_{0.06}$	$Sn_{0.974}Pb_{0.026}Se_{0.957}I_{0.005}$	49.66	48.77	1.32	0.25
0.05	$Sn_{0.95}Pb_{0.05}Se_{0.85}I_{0.10}$	$Sn_{0.958}Pb_{0.042}Se_{0.954}I_{0.005}$	48.92	48.68	2.14	0.26

Figure 2(a) shows XRD patterns of $Sn_{1-x}Pb_xSe_{0.95-2x}I_{2x}$ (x = 0, 0.01, 0.03, and 0.05) along the // direction in a 2θ range from 20° to 70°. All the peaks can be indexed as α-SnSe with a space group of *Pnma* (PDF#48-1224) [20], and no impurity phase can be observed within the detection limit of the XRD spectrometer, indicating all samples have a single SnSe phase with an orthorhombic crystal structure and lattice parameters of a = 11.37 Å, b = 4.19 Å, and c = 4.44 Å. The strongest peak corresponds to the (111) plane, which is different from the XRD results along the □ direction (refer to **Figure S1(a)** in the Supporting Information that the (400) is the strongest peak), indicating the anisotropy of polycrystalline SnSe. The magnified XRD patterns of (111) peaks are shown in **Figure 2(b)**. As can be seen, the peaks of the doped samples slightly shift toward a small angle, suggesting an expansion of the crystal cell. Because Pb^{2+} has a much larger ionic radius of 1.20 Å than Sn^{2+} (0.93 Å) while I^- possesses a larger ionic radius of 2.16 Å than Se^{2-} (1.84 Å), such an expansion in the crystal cell is reasonable, confirming the successful doping of Pb and I. In addition, a similar left-shift of (400) peaks can also be observed in the XRD patterns along the ⍰ direction (refer to **Figure S1(b)**), double confirming the expansion of the crystal cell by Pb and I co-doping.

Figure 2(c) shows a FE-SEM image of $Sn_{0.97}Pb_{0.03}Se_{0.89}I_{0.06}$ pellet fractured along the // direction ($x = 0.03$). The fractured surface shows a typical layered morphology, which explains the anisotropy observed in XRD patterns. SEM images of pellets along the // direction for x = 0, 0.01 and 0.05 are shown in **Figure S2(a-c)**, and SEM image of pellet ($x = 0.05$) along the ⍰ direction can be referred to **Figure S2(d)**. **Figure 2(d)** shows a Cs-corrected STEM high-angle annular dark-field (HAADF) image of $Sn_{0.97}Pb_{0.03}Se_{0.89}I_{0.06}$, from which grain boundaries can be clearly observed. **Figure 2(e)** shows corresponding EDS maps for Sn, Se, Pb, and I, confirming the homogeneous doping of both Pb and I at a microscale. EDS maps based on SEM back-scattered electron (BSE) image taken from the polished surface of $Sn_{0.97}Pb_{0.03}Se_{0.89}I_{0.06}$ pellet can be referred to **Figure S3**, double confirming the homogeneous distribution of Sn, Se, Pb, and I. **Figure 2(f)** is a high-resolution Cs-corrected STEM-HAADF image of $Sn_{0.97}Pb_{0.03}Se_{0.89}I_{0.06}$, in which a typical grain boundary is clearly seen. Some lattice contrast can be seen in the grains, which may be caused by the doping of Pb and I. **Figure 2(g)** shows a high-resolution transmission electron microscopy (HRTEM) image of $Sn_{0.97}Pb_{0.03}Se_{0.89}I_{0.06}$, in which a typical lattice contrast can be observed. The insets show the corresponding fast Fourier transform (FFT) pattern (top-right) and an intensity line profile (bottom-right) taken from the pink dashed line. The FFT pattern indicates that the lattice is viewed along the [001] direction, confirming the crystal nature of SnSe; while the intensity line profile confirms the lattice contrast that caused by the Pb/I co-doping. **Figure 2(h)** shows a high-resolution Cs-corrected STEM-HAADF image of $Sn_{0.97}Pb_{0.03}Se_{0.89}I_{0.06}$, in which the lattice contrasts can be clearer observed as indicated by the arrows. These results confirm that Pb and I were successfully doped into the SnSe lattice.

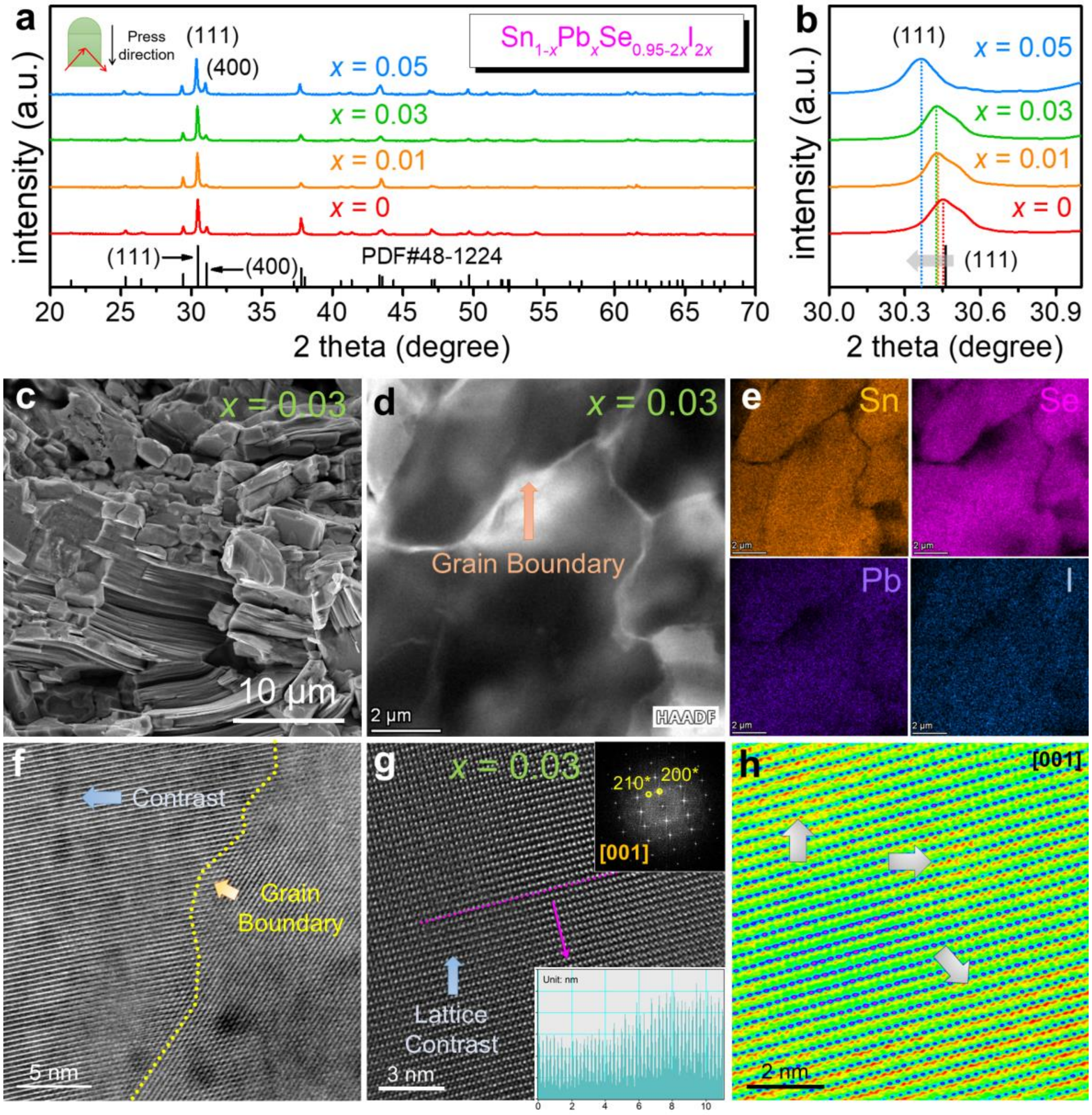

Figure 2. (a) X-ray diffraction (XRD) patterns of $Sn_{1-x}Pb_xSe_{0.95-2x}I_{2x}$ (x = 0, 0.01, 0.03, and 0.05) along the // direction in a 2θ range from 20° to 70°. (b) Magnified XRD patterns of (111) peaks. (c) Field emission scanning electron microscopy (FE-SEM) images of $Sn_{0.97}Pb_{0.03}Se_{0.89}I_{0.06}$ along the // direction (x = 0.03). (d) Spherical aberration-corrected (Cs-corrected) scanning transmission electron microscopy (STEM) high-angle annular dark-field (HAADF) image of $Sn_{0.97}Pb_{0.03}Se_{0.89}I_{0.06}$. (e) Corresponding energy dispersive spectrometer (EDS) maps for Sn, Se, Pb, and I. (f) High-resolution Cs-corrected STEM-HAADF image of $Sn_{0.97}Pb_{0.03}Se_{0.89}I_{0.06}$ showing a typical grain boundary. (g) High-resolution transmission electron microscopy (HRTEM) image of $Sn_{0.97}Pb_{0.03}Se_{0.89}I_{0.06}$ showing a typical lattice contrast. The insets show the corresponding fast Fourier transform (FFT) pattern (top-right) and an intensity line profile

(bottom-right) taken from the pink dashed line. (h) High-resolution Cs-corrected STEM-HAADF image of $Sn_{0.97}Pb_{0.03}Se_{0.89}I_{0.06}$ showing typical lattice contrasts indicated by arrows.

Figure 3(a) compares temperature-dependent S of $Sn_{1-x}Pb_xSe_{0.95-2x}I_{2x}$ (x is 0, 0.01, 0.03, and 0.05), measured along the // direction. It is clearly seen that after doping with Pb and I, n-type SnSe is successfully realized. A high absolute S value of ~429.0 μV K^{-1} at 773 K can be seen when $x = 0.01$. **Figure 3(b)** shows temperature-dependent σ of $Sn_{1-x}Pb_xSe_{0.95-2x}I_{2x}$ (x is 0, 0.01, 0.03, and 0.05). With increasing the doping concentration of Pb and I, σ is significantly enhanced, mainly derived from the extra electron carriers provided by the I^- that substitute Se-sites. **Figure 3(c)** shows the determined $S^2\sigma$ of $Sn_{1-x}Pb_xSe_{0.95-2x}I_{2x}$ (x is 0, 0.01, 0.03, and 0.05). An optimized $S^2\sigma$ of ~5.1 μW cm^{-1} K^{-2} at 773 K can be observed when $x = 0.03$, derived from the coupling of S and σ. **Figure 3(d)** shows x-dependent n and μ of $Sn_{1-x}Pb_xSe_{0.95-2x}I_{2x}$ (x is 0, 0.01, 0.03, and 0.05). With increasing the doping concentration of Pb and I, n is significantly enhanced, while μ is first decreased due to the p-n transition from $x = 0$ to $x = 0.01$, and then increased due to the increase of n. **Figure 3(e)** shows calculated effective mass m^* and deformation potential E_{def} of $Sn_{1-x}Pb_xSe_{0.95-2x}I_{2x}$ as a function of x value. As can be seen, with increasing the x until $x = 0.03$, m^* reaches to the maximized value while E_{def} reach to the minimized value in our samples, indicating that a couple of S and σ has been realized, leading to an optimized $S^2\sigma$. **Figure 3(f)** compares temperature-dependent κ of $Sn_{1-x}Pb_xSe_{0.95-2x}I_{2x}$ (x is 0, 0.01, 0.03, and 0.05) measured along the // direction. A low κ of ~0.43 W m^{-1} K^{-1} at 773 K can be observed when $x = 0.01$, indicating a significant reduction of κ compared with pristine SnSe (κ of 0.54 W m^{-1} K^{-1}). **Figure 3(g)** shows determined temperature-dependent κ_l of $Sn_{1-x}Pb_xSe_{0.95-2x}I_{2x}$ (x is 0, 0.01, 0.03, and 0.05). The achieved κ_l is close to the corresponding κ, indicating that κ_l dominates κ. The reduction of κ_l can be attributed to the Pb and I co-doping, since both Pb and I act as point-defect-based phonon scattering centers to strengthen the short-wavelength phonon scattering. The calculated temperature-dependent Lorenz number L and κ_e

are shown in **Figure S4**. **Figure 3(h)** shows 1000/T-dependent κ_l of $Sn_{1-x}Pb_xSe_{0.95-2x}I_{2x}$ (x is 0, 0.01, 0.03, and 0.05). It is clearly seen that all the plots show a linear relationship, indicating that the Umklapp phonon scattering dominates the phonon scattering [19, 22, 24, 35]. **Figure 3(i)** compares determined temperature-dependent ZT of $Sn_{1-x}Pb_xSe_{0.95-2x}I_{2x}$ (x is 0, 0.01, 0.03, and 0.05). A promising ZT of 0.9 at 773 K can be achieved by co-doping with 3 % Pb and 6 % I ($x = 0.03$), indicating that Pb and I co-doping benefit the high thermoelectric performance of n-type SnSe. The thermoelectric performance of $Sn_{1-x}Pb_xSe_{0.95-2x}I_{2x}$ measured or determined along the ⍰ direction can be referred to **Figure S5** in the supporting information. A peak ZT of ~0.6 can be seen in $Sn_{0.97}Pb_{0.03}Se_{0.89}I_{0.06}$ ($x = 0.3$), which is lower than that achieved along the // direction. In addition, the real compositions for the Pb/I co-doped SnSe samples after electrical and thermal property test can be referred to **Table S2** in the supporting information, evaluated by EPMA, and the differential scanning calorimetry (DSC) test of the sample $Sn_{0.97}Pb_{0.03}Se_{0.89}I_{0.06}$ is also shown in **Figure S6(a)**. These results indicate that our samples possess high thermal stability.

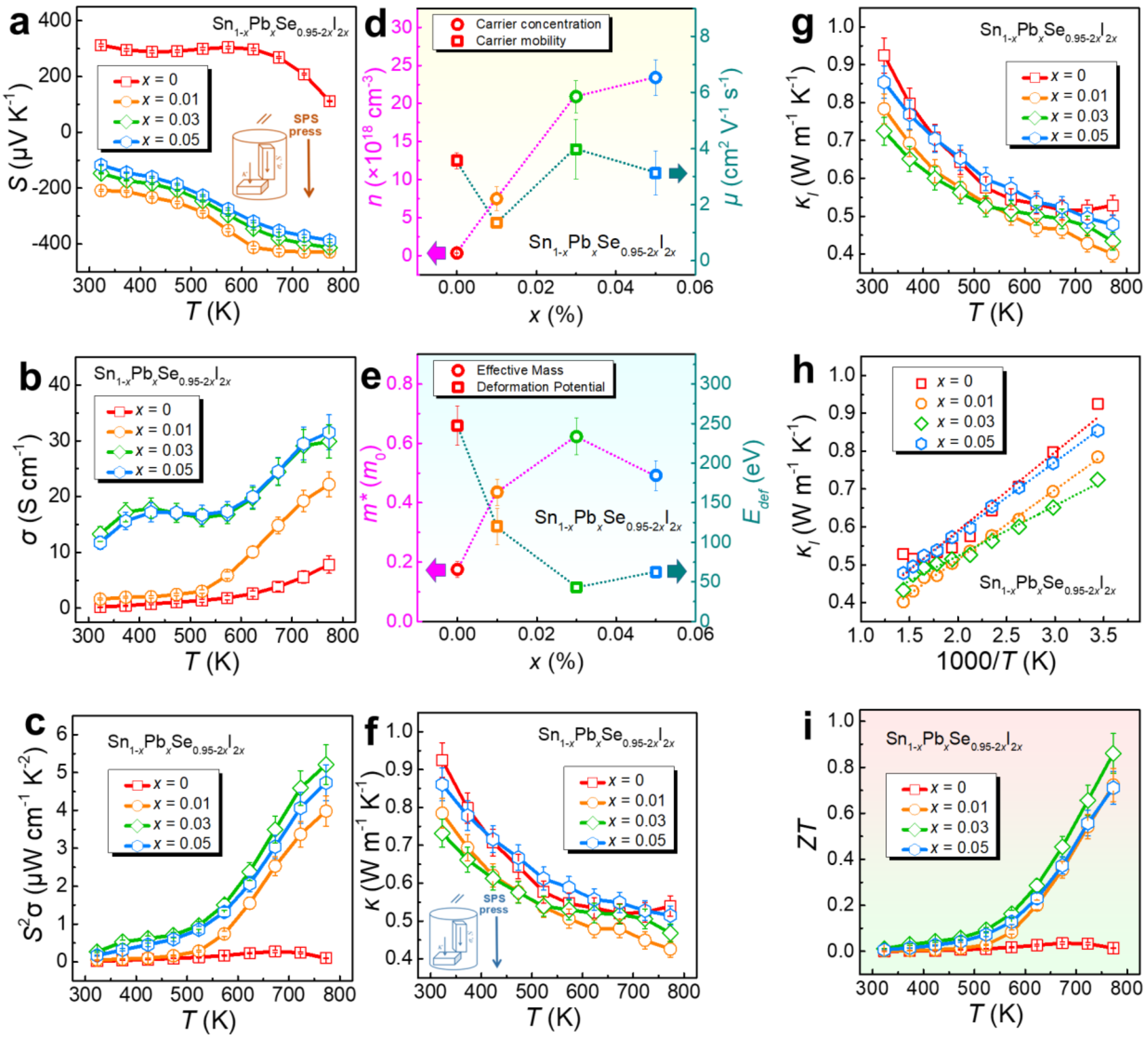

Figure 3. *T*-dependent (a) *S*, (b) *σ*, and (c) $S^2\sigma$ of $Sn_{1-x}Pb_xSe_{0.95-2x}I_{2x}$. *x*-dependent room-temperature (d) *n* and *μ*, and (e) *m** and E_{def} of $Sn_{1-x}Pb_xSe_{0.95-2x}I_{2x}$. *T*-dependent (f) *κ* and (g) κ_l of $Sn_{1-x}Pb_xSe_{0.95-2x}I_{2x}$. (h) 1000/*T*-dependent κ_l of $Sn_{1-x}Pb_xSe_{0.95-2x}I_{2x}$, and (i) *T*-dependent *ZT* of $Sn_{1-x}Pb_xSe_{0.95-2x}I_{2x}$. Here *x* is 0, 0.01, 0.03, and 0.05, respectively. All properties are measured or determined along the // direction.

To illustrate the mechanism of the increased *n* and *σ* by Pb/I co-doping, we performed DFT calculations on the electronic band structures for SnSe before and after Pb-doping, I-doping, and Pb/I co-doping. **Figure 4(a-d)** show calculated band structures of pristine, Pb-doped, I-doped, and Pb/I co-doped SnSe, respectively, and **Figure 4(e-h)** show their corresponding DOS. Interestingly, before and after Pb^{2+} replacing Sn^{2+}, the band structures and DOS are almost identical with the only difference being that the bands in the pristine SnSe lattice slightly split after Pb atoms are introduced. In contrast, after I^- replacing Se^{2-}, Fermi level moves into the conduction band, making the material n-type with significantly increased electron concentration. Therefore, it can be concluded that I dopant can introduce more electrons in SnSe.

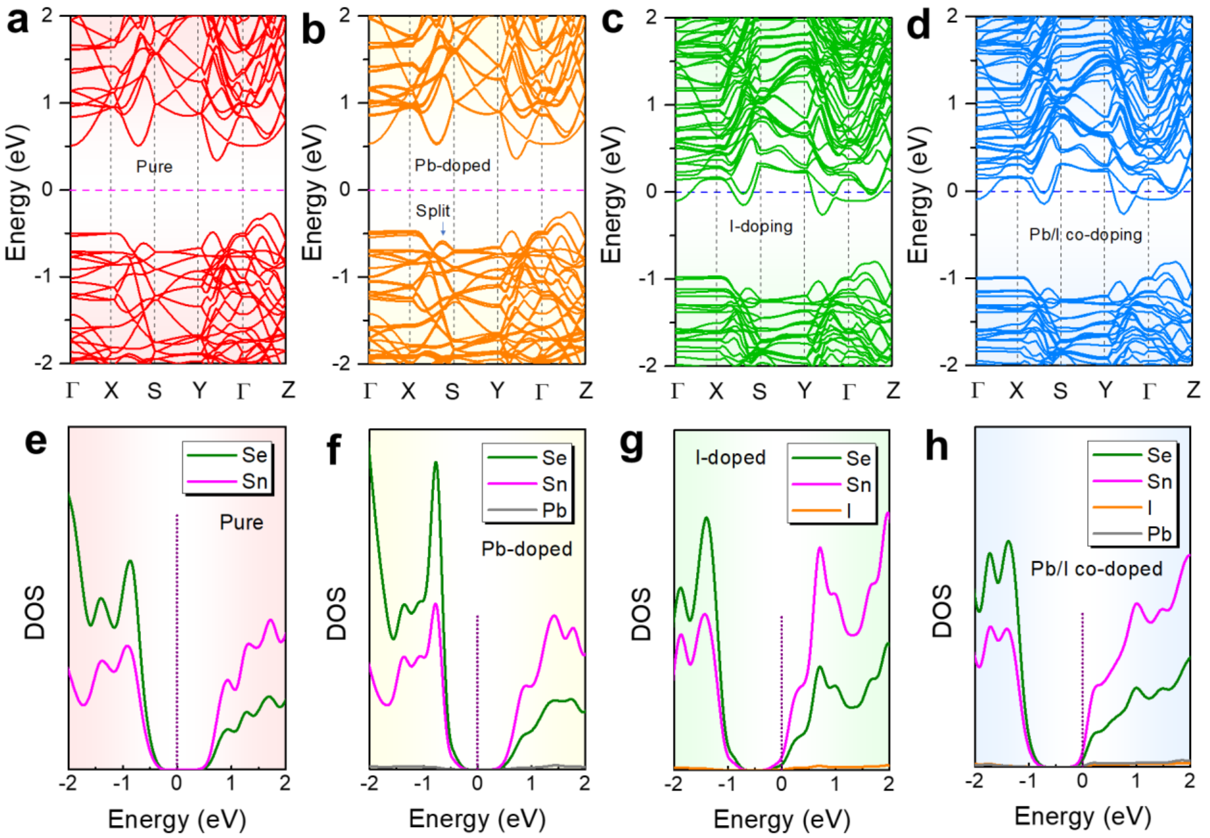

Figure 4. Calculated band structures of (a) pristine, (b) Pb-doped, (c) I-doped, and (d) Pb/I co-doped SnSe, and corresponding DOS of (e) pristine, (f) Pb-doped, (g) I-doped, and (h) Pb/I co-doped SnSe, respectively.

To further improve the thermoelectric performance of n-type polycrystalline SnSe, we introduce 2D WSe_2 nanoplates with an average size of ~393.8 nm (refer to **Figure S7**) as nanoinclusions in the $Sn_{0.97}Pb_{0.03}Se_{0.89}I_{0.06}$ matrix with different contents, described as $Sn_{0.97}Pb_{0.03}Se_{0.89}I_{0.06}$-$y$ % WSe_2 (y = 0, 0.5, 1.0, 2.0, and 4.0). Because WSe_2 has a much higher melting point of >1473 K than SnSe (1134 K) [3], WSe_2 nanoinclusions can be well maintained during solid-state reaction and SPS process. The DSC test of the sample $Sn_{0.97}Pb_{0.03}Se_{0.89}I_{0.06}$ + 1 % WSe_2 is shown in **Figure S6(b)**, indicating high thermal stability. **Figure 5(a)** shows XRD patterns of $Sn_{0.97}Pb_{0.03}Se_{0.89}I_{0.06}$-$y$ % WSe_2 along the // direction in a 2θ range from 10° to 60°. For the samples with $y < 4.0$, all the peaks can be indexed as α-SnSe with a space group of *Pnma* (PDF#48-1224) and lattice parameters of $a = 11.37$ Å, $b = 4.19$ Å, and $c = 4.44$ Å [20], and no obvious impurity phase can be observed within the detection limit of the XRD spectrometer. In contrast, WSe_2 nanophase can be detected only when $y = 4$, indicating the lower-content of WSe_2 nanoinclusions in SnSe may be out of the detection limit of the XRD spectrometer. The XRD patterns of $Sn_{0.97}Pb_{0.03}Se_{0.89}I_{0.06}$-$y$ % WSe_2 along the ⍰ direction can be referred to **Figure S8(a)**. **Figure 5(b)** shows FE-SEM image of $Sn_{0.97}Pb_{0.03}Se_{0.89}I_{0.06}$-1 % WSe_2 fractured along the // direction, from which typical layered morphology can be seen, similar to the samples before embedding WSe_2 nanoinclusions. However, it is still failed to observe the WSe_2 nanoinclusions under such a "large" scale by SEM, therefore TEM-based characterizations are needed. FE-SEM images of $Sn_{0.97}Pb_{0.03}Se_{0.89}I_{0.06}$-$y$ % WSe_2 for $y = 0.5$, 2.0, and 4.0 can be referred to **Figure S8(b-d)**. **Figure 5(c)** shows a Cs-corrected STEM-HAADF image of $Sn_{0.97}Pb_{0.03}Se_{0.89}I_{0.06}$-1 % WSe_2, from which a typical inclusion with different contrast from the surrounding area can be clearly seen. **Figure 5(d)** shows a Cs-corrected STEM-HAADF image magnified from **Figure 5(c)** (the square area). The inclusion has an irregular shape with a dimension of <300 nm, indicating a typical nanoinclusion. **Figure 5(e)** shows a high-resolution Cs-corrected STEM-HAADF image magnified from **Figure 5(d)** (the square area). Clearly, the lattice of the secondary phase is distinct from the dominant phase, and the dominant phase can be indexed as SnSe viewed along the [021] direction by the inset FFT pattern. There are also obvious lattice distortions found in the secondary phase. **Figure 5(f)** shows a high-resolution Cs-corrected STEM-HAADF image of SnSe phase viewed along the [021] direction, in which the overlays show Se or I atoms in blue and Sn or Pb atoms in yellow, all indicating the typical orthorhombic α-SnSe phase. **Figure 5(g-j)** show EDS maps on the interface for total elements, Sn, W, and Se, respectively. As shown in the contrast, the secondary nanophase can be indexed as WSe_2. The EDS results of $Sn_{0.97}Pb_{0.03}Se_{0.89}I_{0.06}$-2 % WSe_2 can be referred to **Figure S9**.

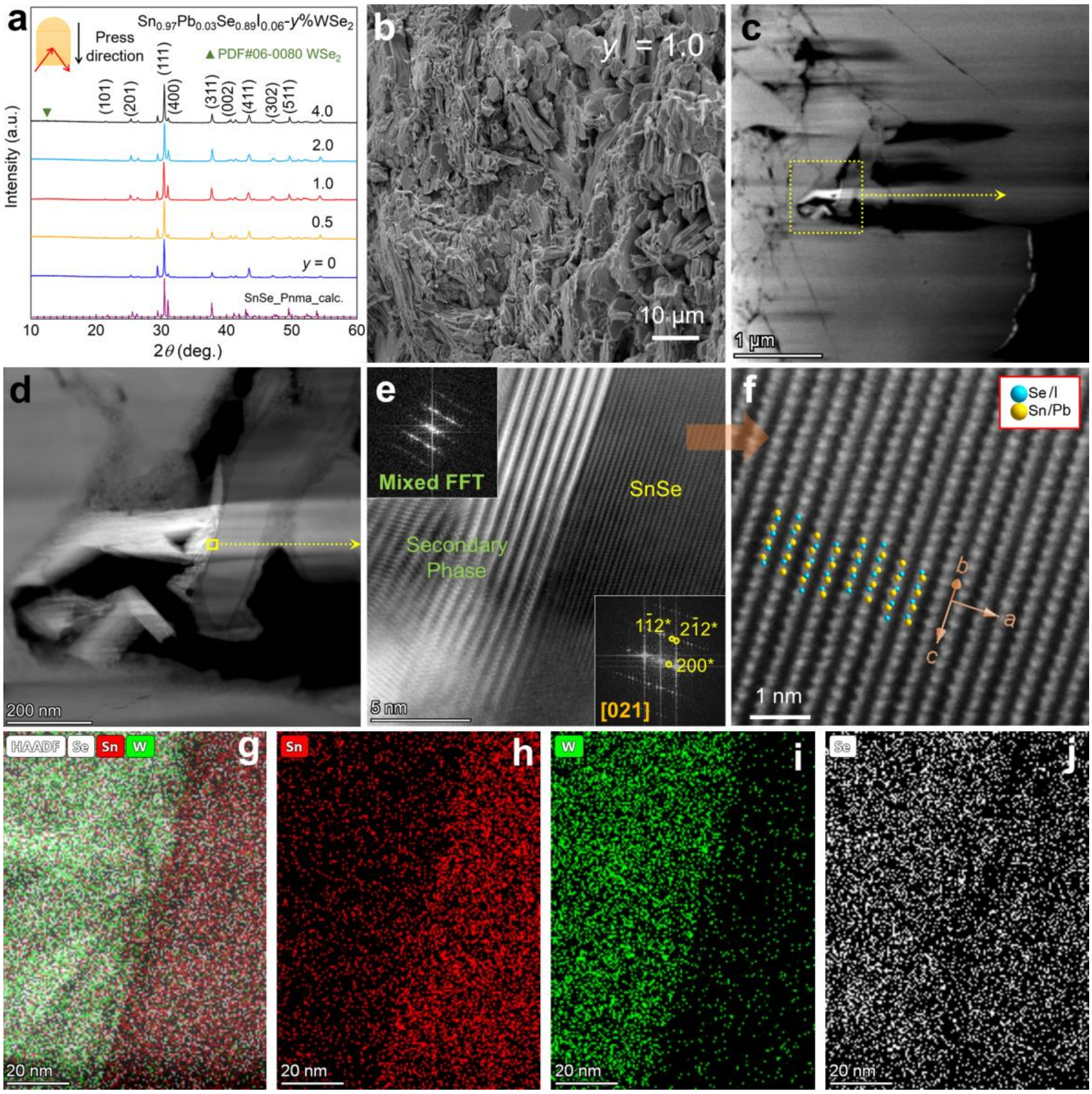

Figure 5. (a) XRD patterns of $Sn_{0.97}Pb_{0.03}Se_{0.89}I_{0.06}$-$y$ % WSe_2 (y = 0, 0.5, 1.0, 2.0, and 4.0) along the // direction in a 2θ range from 10° to 60°. (b) FE-SEM image of $Sn_{0.97}Pb_{0.03}Se_{0.89}I_{0.06}$-1 % WSe_2 along the // direction. (c) Cs-corrected STEM-HAADF image of $Sn_{0.97}Pb_{0.03}Se_{0.89}I_{0.06}$-1 % WSe_2. (d) Magnified Cs-corrected STEM-HAADF image taken from (c) to show the nanoinclusion. (e) Magnified high-resolution Cs-corrected STEM-HAADF image taken from (d) to show the interface between SnSe phase and the secondary phase. The SnSe phase can be indexed as viewed along the [021] direction, indicated by the inset FFT

pattern. (f) HR-STEM-HAADF image of the SnSe phase along the [021] direction, and EDS maps on the interface for (g) total, (h) Sn, (i) W, and (j) Se, respectively.

Figure 6(a-c) compares temperature-dependent S, σ, and $S^2\sigma$ of $Sn_{0.97}Pb_{0.03}Se_{0.89}I_{0.06}$-$y$ % WSe_2 ($y = 0$, 0.5, 1.0, and 2.0.) measured along the // direction. As can be seen, after introducing WSe_2 nanoinclusions, the absolute S is significantly enhanced, benefiting from the "depletion layer effect" driven by the p-n junction and potentially reduced n. A high absolute S value of ~470.7 μV K^{-1} at 790 K is observed when $y = 1$. With increasing the content of 2D WSe_2 nanoinclusions, σ is reduced. Considering that 2D WSe_2 nanoinclusions obviously increase the density of phase boundary, most of the low-energy carriers were scattered at these phase boundaries, leading to a lower σ. As a result, an optimized $S^2\sigma$ of ~5.9 μW cm^{-1} K^{-2} at 790 K can be observed when $y = 1$, derived from the coupling of S and σ. **Figure 6(d)** shows n and μ of $Sn_{0.97}Pb_{0.03}Se_{0.89}I_{0.06}$-$y$ % WSe_2 as a function of y value. With increasing the content of WSe_2 nanoinclusions, n is reduced, explaining the reduction of σ and the improvement of S; while μ is fluctuated. The introduction of p-type 2D WSe_2 nanoinclusions induces high-density WSe_2/SnSe interfaces that act as p-n junctions, which arises the "depletion layer effect" and leads to the decrease of n. **Figure 6(e)** shows calculated effective mass m^* and deformation potential E_{def} of $Sn_{0.97}Pb_{0.03}Se_{0.89}I_{0.06}$-$y$ % WSe_2 as a function of y value. It can be seen that with increasing the y, m^* is reduced, indicating an enhanced absolute S (for n-type); while E_{def} is increased, indicating the increase of μ. In fact, the calculated m^* and E_{def} for $Sn_{0.97}Pb_{0.03}Se_{0.89}I_{0.06}$-$y$ % WSe_2 can only be used for reference since the samples have more than one phase. **Figure 6(f)** illustrates the mechanism of depletion layer effect by WSe_2/SnSe phase boundaries that act as p-n junctions, in which the bandgap value of p-type WSe_2 (0.87 eV) comes from the calculated band structure of WSe_2 (refer to **Figure S10**), and the bandgap value of n-type SnSe (0.59 eV) comes from the calculated band structure of Pb/I co-doped SnSe (refer to **Figure 4**). The p-n junctions result in build-in electric fields around the phase boundaries, which are responsible for the fluctuation of μ. In addition, the band alignment at the interface between the p-type WSe_2 and n-type Pb/I co-doped SnSe results in an ultrahigh interface potential, which act as a type of "depletion layer", significantly block the carriers and in turn reduce n and enhance S. Besides, the increased m^* also confirms the strong blocking effect since the carriers with relatively low energy are considerably blocked.

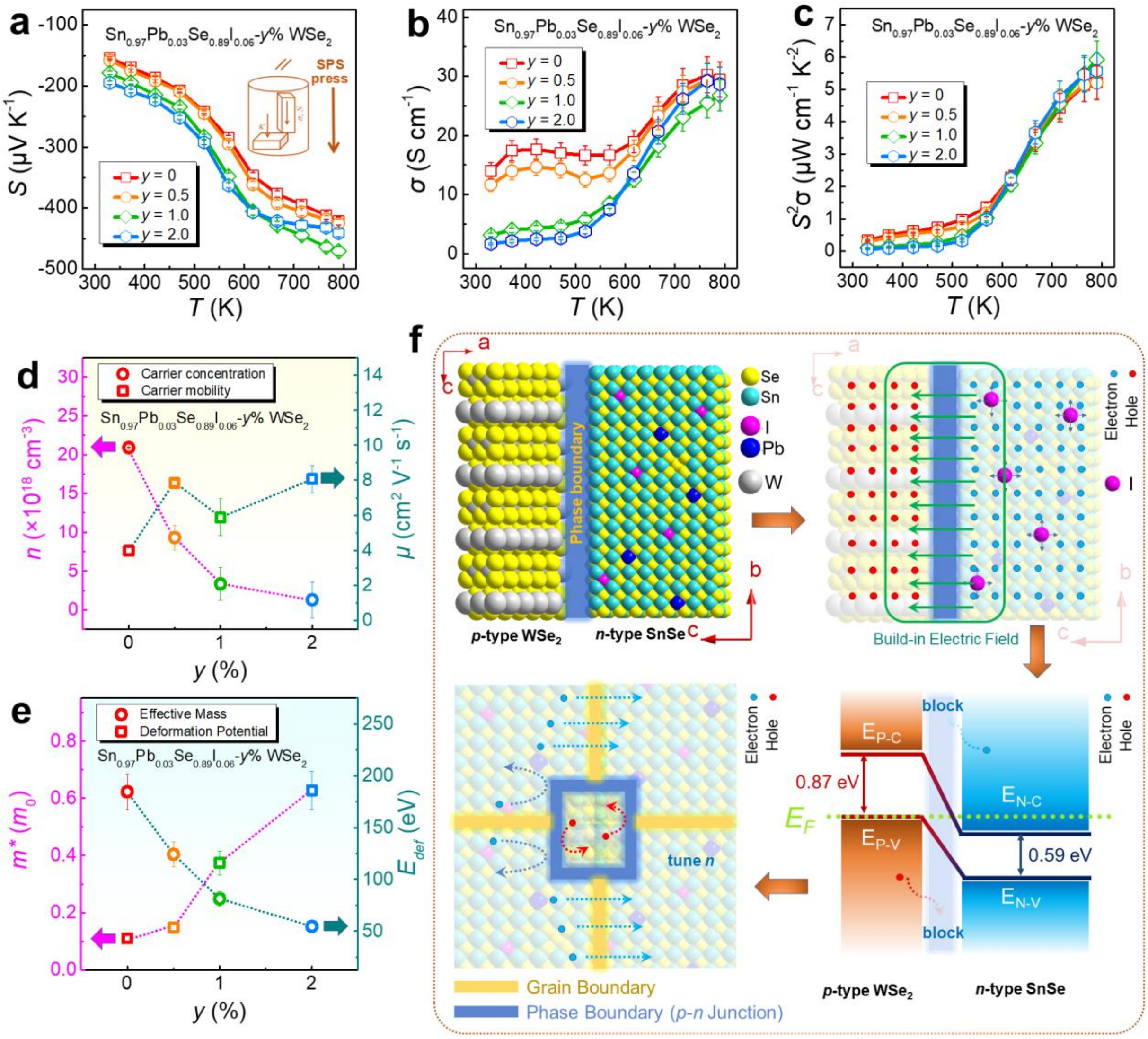

Figure 6. T-dependent (a) S, (b) σ, and (c) $S^2\sigma$ of $Sn_{0.97}Pb_{0.03}Se_{0.89}I_{0.06}$-$y$ % WSe_2. y-dependent room-temperature (d) n and μ, and (e) m^* and E_{def} of $Sn_{0.97}Pb_{0.03}Se_{0.89}I_{0.06}$-$y$ % WSe_2. (f) Illustration of build-in electric field and depletion layer effect at the phase boundaries (p-n junctions) between the p-type WSe_2 and n-type Pb/I co-doped SnSe.

Figure 7(a-b) compare temperature-dependent κ and κ_l of $Sn_{0.97}Pb_{0.03}Se_{0.89}I_{0.06}$-$y$ % WSe_2 measured along the // direction. The calculated temperature-dependent Lorenz number L and κ_e can be referred to **Figure S11**. A low κ of ~0.35 W m^{-1} K^{-1} at 790 K can be seen when y = 1, indicating a significant reduction compared with the samples without WSe_2. The reduction of κ_l can be attributed to the introducing of WSe_2 nanoinclusions, since 2D WSe_2 has an ultralow intrinsic κ (only 0.05 W m^{-1} K^{-1}) [41], and these nanoinclusions provide high-density phase boundaries that act as extra phonon scattering sources targeting to scatter the long-wavelength phonons. In addition, these nanoinclusions can also act as phonon scattering centers and cause significant strain fields in the surrounding SnSe lattices, further strengthening the phonon scattering and in turn reducing the κ_l. Callaway model was employed to calrify for the specific frequency range with phonon-scattering centers for mid-to-long-wavelength phonons:

$$\kappa_l = \frac{4\pi\, {k_B}^4\, T^3}{v h^3} \int_0^{\frac{\theta_D}{T}} \frac{z^4 \exp(z)}{\tau_T^{-1}[\exp(z)-1]^2} \mathrm{d}z \tag{1}$$

where k_B is the Boltzmann constant, v is the sound speed, and h is the Planck's constant. In this system, phonon scattering mechanism influences the phonon transport, including impurity/point defect phonon scattering, phonon-phonon Umklapp scattering, phonon scattering by nanoinclusions, and phase boundary phonon scattering. In calculation process, only dominating scattering mechanisms are considered in this work, including the impurity/point defect phonon scattering τ_{im}^{-1} (PD), phonon-phonon Umklapp scattering τ_U^{-1} (U), phase boundary phonon scattering τ_{pb}^{-1} (PB) and electron-phonon scattering τ_{ep}^{-1} (E). Therefore, the total phonon relaxation time can be simplified as:

$$\tau_T^{-1} = \tau_{im}^{-1} + \tau_U^{-1} + \tau_{ep}^{-1} + \tau_{pb}^{-1} \tag{2}$$

or:

$$\tau_T^{-1} = A\omega^4 + \mathrm{B}\omega^2 \mathrm{T} \exp\left(-\frac{\theta_D}{3T}\right) + C\omega^2 + \frac{v}{d} \tag{3}$$

where ω and d are the phonon frequency and the average spatial distance among the WSe_2 nanoinclusions in n-type Pb/I co-doped SnSe matrix. The value of v was measured and θ_D was calculated based on the measured v value (see **Table S3** in the supporting file). The parameters A and B were determined by fitting κ_l data, as listed in **Table S3**. By using the obtained parameters, κ_l for the typical composites of n-type Pb/I co-doped SnSe matrix with p-type 2D-WSe_2 nanoinclusion were calculated through Formula 1 and Formula 2. It can be clearly seen that calculated κ_l is in good agreement with experimental results. It is noted that the obtained average spatial distance d among the nanoinclusions is around 218 nm for the composite sample with y = 1 wt.%, which could be underestimated since we neglected some other scattering mechanisms in the calculations as mentioned above. The parameters used in the calculations for Debye model are given in **Table S3**. It is noted that the obtained average spatial distance d among the nanoinclusions is in good agreement for the composite sample with y = 0.5 and 1.0 wt.%. However, further increase in content y causes to increase the average spatial distance, which could be ascribed to the agglomeration effect of high quantity of content in matrix. **Figure 7(c)** shows 1000/T-dependent κ_l of $Sn_{0.97}Pb_{0.03}Se_{0.89}I_{0.06}$-$y$ % WSe_2. All plots show a linear relationship, indicating that the Umklapp phonon scattering still dominate the phonon scattering after introducing WSe_2 [19, 22, 24, 35].

Figure 7(d) compares determined temperature-dependent ZT of $Sn_{0.97}Pb_{0.03}Se_{0.89}I_{0.06}$-$y$ % WSe_2. A high ZT of ~1.35 at 790 K can be achieved by introducing 1 % WSe_2 nanoinclusions, which ranks as one of the highest values compared to the previously reported works, as shown in **Table 2** and **Figure S12** [35-40, 49-61]. The thermoelectric performance of $Sn_{0.97}Pb_{0.03}Se_{0.89}I_{0.06}$-$y$ % WSe_2 (y = 0 and 1) measured or determined along the ⍰ direction can be seen in **Figure S13** in the supporting information. As can be seen, a peak ZT of ~0.65 can be observed in $Sn_{0.97}Pb_{0.03}Se_{0.89}I_{0.06}$-1 % WSe_2, which is lower than that achieved along the // direction. Furthermore, our results show significantly high repeatability, as confirmed by **Figure S14**.

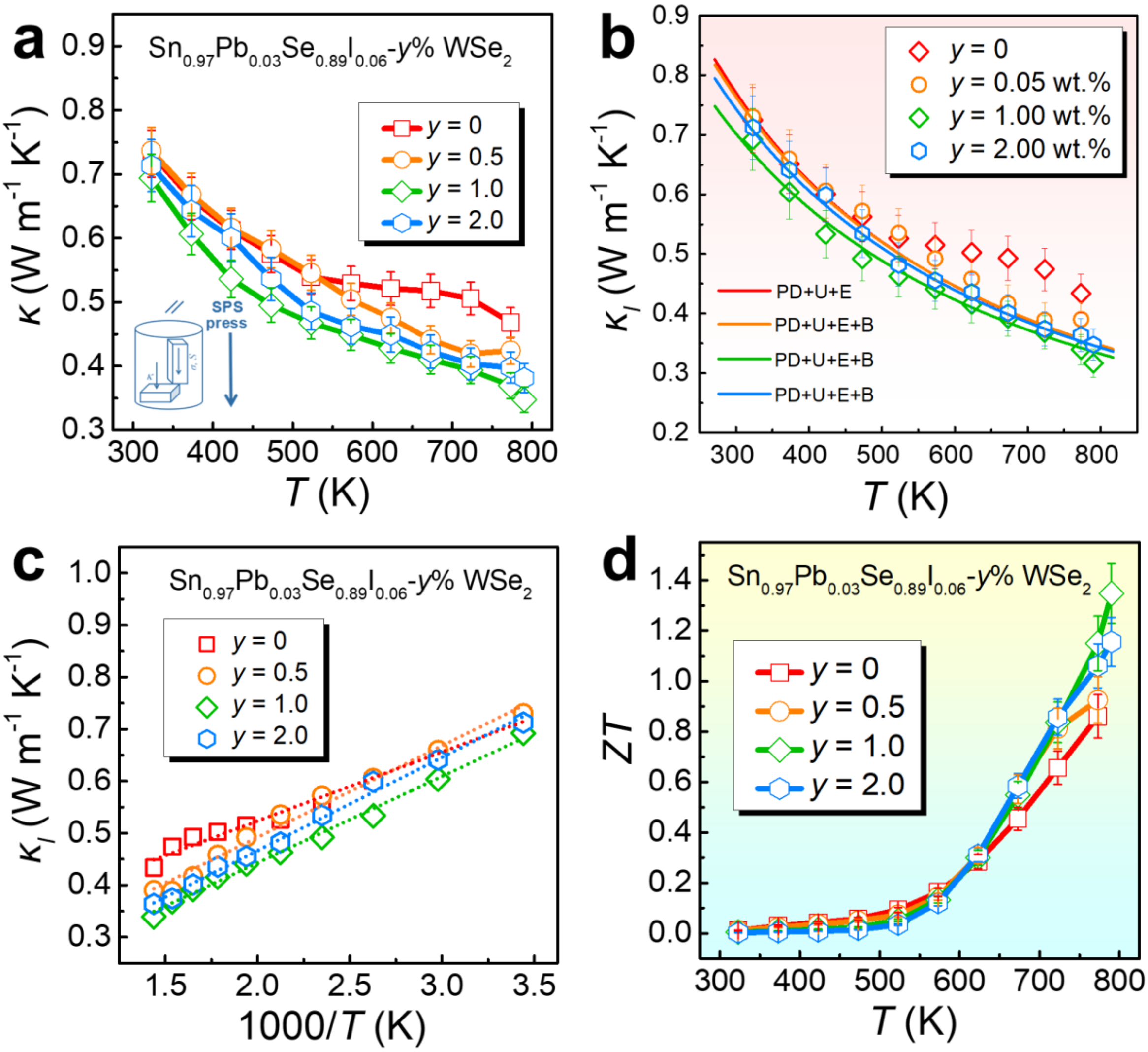

Figure 7. *T*-dependent (a) κ and (b) κ_l of $Sn_{0.97}Pb_{0.03}Se_{0.89}I_{0.06}$-*y* % WSe_2. The calculated κ_l using Callaway model are included in (b), including impurity/point defect phonon scattering τ_{im}^{-1} (PD), phonon-phonon Umklapp scattering τ_U^{-1} (U), phase boundary phonon scattering τ_{pb}^{-1} (PB) and electron-phonon scattering τ_{ep}^{-1} (E). (c) 1000/*T*-dependent κ_l of $Sn_{0.97}Pb_{0.03}Se_{0.89}I_{0.06}$-*y* % WSe_2. (d) *T*-dependent *ZT* of $Sn_{0.97}Pb_{0.03}Se_{0.89}I_{0.06}$-*y* % WSe_2. Here *y* is 0, 0.5, 1.0, and 2.0, respectively. All the properties are measured or determined along the // direction.

Table 2. A summary of n-type polycrystalline bulk SnSe.

Materials	***ZT***	***T* (K)**	***σ* (S cm^{-1})**	***S* (μV K^{-1})**	***S*^{2}*σ* (μW cm^{-1} K^{-2})**	***κ* (W m^{-1} K^{-1})**	**Ref.**
$SnSe_{0.87}S_{0.1}I_{0.03}$	~1.0	773	~16	~-500	~4.0	~0.36	[49]
$SnSe_{0.95}$-0.4 % $BiCl_3$	0.7	793	~29	~-414	~5.0	~0.6	[50]
$SnSb_{0.02}Se_{0.96}$	1.1	773	~39	-247	~2.4	~0.17	[35]
$SnSe_{0.95}$-3 % $PbBr_2$	0.54	793	~36	~-360	~4.7	~0.72	[51]
$Sn_{0.97}Re_{0.03}Se_{0.93}Cl_{0.02}$	1.5	798	~30	~-430	~5.8	~0.3	[36]
$Sn_{0.90}Pb_{0.15}Se_{0.95}Cl_{0.05}$	1.2	823	~50	~-360	~6.7	~0.46	[37]
$Sn_{0.90}Pb_{0.10}Se_{0.97}Br_{0.03}$	1.2	773	~35	~-400	~5.6	~0.37	[38]
$Sn_{0.74}Pb_{0.20}Ti_{0.06}Se$	0.4	773	~15	-450	3.0	~0.58	[52]
$SnSe_{0.9}Br_{0.1}$	1.3	773	~28	~-400	~4.5	~0.26	[39]
$Sn_{1.005}Se_{0.94}Br_{0.06}$	1.5	783	~32	~-460	~6.8	~0.36	[40]
Oxygen-isolated $SnSe_{0.97}Br_{0.03}$	1.0	773	~20	~-500	~5.0	~0.36	[53]
$(SnSe)_{0.1}(PbSe)_{0.9}$	1.0	773	~490	~-180	~16.5	~1.20	[54]
$Sn_{0.97}Bi_{0.03}Se$	-	723	~3.0	~-390	~0.45	-	[55]
$Sn_{0.94}Bi_{0.06}Se$	0.025	723	~5.5	~-190	~0.2	~0.53	[56]
$SnSe_{0.9375}Te_{0.0625}$	-	673	~3.6	~-280	~0.3	-	[57]
$SnSe_{0.98}$	~0.07	773	~3.0	~-380	~0.4	~0.5	[58]
$Sn_{0.8}Sb_{0.2}Se$	0.3	908	~100	~-125	~1.0	~0.46	[59]
SnSe + SiC	0.125	300	~7.3	-581	~2.5	~0.6	[60]
$SnSe_{0.94}Cl_{0.06}$ + $SnSe_2$	0.56	773	~32	~-300	~2.9	~0.43	[61]
$Sn_{0.97}Pb_{0.03}Se_{0.89}I_{0.06}$-*y* % WSe_2, **This work**	1.35	790	26.6	-470.7	5.9	0.35	

4. Conclusion

In this work, a high *ZT* of ~1.35 at 790 K has been realized in n-type polycrystalline SnSe by a combination of Pb/I co-doping and introducing 2D WSe_2 nanoinclusions to form WSe_2/SnSe p-n junctions. Calculation results confirm the I-doping shifts the Fermi level up into the conduction bands, making the system n-type. A high $S^2\sigma$ of ~5.9 μW cm^{-1} K^{-2} is achieved by tuning a n of 3.34×10^{18} cm^{-3} through 3 % I-doping and carrier blocking by introducing WSe_2/SnSe p-n junctions (1 % WSe_2). Meanwhile, a low κ of ~0.35 W m^{-1} K^{-1} is obtained, benefited from the strengthened phonon scattering at Pb and I that act as point defects, as well as the high-density phase boundaries by introducing WSe_2 nanoinclusions. This study indicates that rational band engineering and nanostructural design possess great potential for securing high thermoelectric performance in n-type polycrystalline SnSe.

Author contributions

Y.X.C., X.L.S., Z.H.Z., P.F. and Z.G.C. designed the experiments; Y.X.C., X.L.S., F.L., W.D.L. and W.Y.C. performed the material synthesis and sample measurement; X.R.L., G.X.L. and J.T.L. performed the theoretical calculation; Y.X.C., X.L.S. and Z.H.Z. conducted the SEM and TEM characterization. Everyone was involved in writing the article.

Conflicts of interest

The authors declare no competing financial interest.

Declaration of competing interest

The authors declare that they have no known competing financial interests or personal relationships that could have appeared to influence the work reported in this paper.

Acknowledgements

This work was financially supported by the National Natural Science Foundation of China (Grant No. 11604212), Guangdong Basic and Applied Basic Research Foundation (Grant No. 2019A1515110107 and 2020A1515010515), Shenzhen Key Lab Fund (ZDSYS 20170228105421966), Australia Research Council, Innovation Centre for Sustainable Steel Project, and USQ Strategic research fund. The authors also are thankful for the assistance on HAADF-STEM observation received from the Electron Microscope Center of the Shenzhen University.

Reference

[1] X. Shi and L. Chen, Nat. Mater. 15 (2016) 691-692.

[2] X.-L. Shi, J. Zou, and Z.-G. Chen, Chem. Rev. 120 (2020) 7399-7515.

[3] Z.-G. Chen, X. Shi, L.-D. Zhao, and J. Zou, Prog. Mater. Sci. 97 (2018) 283-346.

[4] G. Tan, L.D. Zhao, and M.G. Kanatzidis, Chem. Rev. 116 (2016) 12123-12149.

[5] X.-L. Shi, H. Wu, Q. Liu, W. Zhou, S. Lu, Z. Shao, M. Dargusch, and Z.-G. Chen, Nano Energy 78 (2020) 105195.

[6] M. Hong, Z.G. Chen, L. Yang, Z.M. Liao, Y.C. Zou, Y.H. Chen, S. Matsumura, and J. Zou, Adv. Energy Mater. 8 (2017) 1702333.

[7] Y. Wu, Z. Chen, P. Nan, F. Xiong, S. Lin, X. Zhang, Y. Chen, L. Chen, B. Ge, and Y. Pei, Joule 3 (2019) 1276-1288.

[8] J. Li, X. Zhang, Z. Chen, S. Lin, W. Li, J. Shen, I.T. Witting, A. Faghaninia, Y. Chen, and A. Jain, Joule 2 (2018) 976-987.

[9] B. Zhong, Y. Zhang, W. Li, Z. Chen, J. Cui, W. Li, Y. Xie, Q. Hao, and Q. He, Appl. Phys. Lett. 105 (2014) 123902.

[10] W. Liu, L. Yang, Z.-G. Chen, and J. Zou, Adv. Mater. 32 (2020) 1905703.

[11] C. Chang, M. Wu, D. He, Y. Pei, C.-F. Wu, X. Wu, H. Yu, F. Zhu, K. Wang, and Y. Chen, Science 360 (2018) 778-783.

[12] L.-D. Zhao, C. Chang, G. Tan, and M.G. Kanatzidis, Energy Environ. Sci. 9 (2016) 3044-3060.

[13] C. Chang, G. Tan, J. He, M.G. Kanatzidis, and L.-D. Zhao, Chem. Mater. 30 (2018) 7355-7367.

[14] M. Jin, X.-L. Shi, T. Feng, W. Liu, H. Feng, S.T. Pantelides, J. Jiang, Y. Chen, Y. Du, J. Zou, and Z.-G. Chen, ACS Appl. Mater. Interfaces 11 (2019) 8051-8059.

[15] Y. Zheng, X.-L. Shi, H. Yuan, S. Lu, X. Qu, W. Liu, L. Wang, K. Zheng, J. Zou, and Z.-G. Chen, Mater. Today Phys. 13 (2020) 100198.

[16] L.-D. Zhao, G. Tan, S. Hao, J. He, Y. Pei, H. Chi, H. Wang, S. Gong, H. Xu, and V.P. Dravid, Science 351 (2016) 141-144.

[17] S. Sassi, C. Candolfi, J.B. Vaney, V. Ohorodniichuk, P. Masschelein, A. Dauscher, and B. Lenoir, Appl. Phys. Lett. 104 (2014) 212105.

[18] X.-L. Shi, W.-Y. Chen, X. Tao, J. Zou, and Z.-G. Chen, Mater. Horiz. (2020). DOI: 10.1039/D0MH00954G.

[19] X. Shi, Z.-G. Chen, W. Liu, L. Yang, M. Hong, R. Moshwan, L. Huang, and J. Zou, Energy Storage Mater. 10 (2018) 130-138.

[20] M. Dargusch, X.-L. Shi, X.Q. Tran, T. Feng, F. Somidin, X. Tan, W. Liu, K. Jack, J. Venezuela, H. Maeno, T. Toriyama, S. Matsumura, S.T. Pantelides, and Z.-G. Chen, J. Phys. Chem. Lett. 10 (2019) 6512-6517.

[21] X.-L. Shi, W.-D. Liu, A.-Y. Wu, V.T. Nguyen, H. Gao, Q. Sun, R. Moshwan, J. Zou, and Z.-G. Chen, InfoMat 2 (2020) 1201-1215.

[22] X.L. Shi, K. Zheng, M. Hong, W.D. Liu, R. Moshwan, Y. Wang, X.-L. Qu, Z.G. Chen, and J. Zou, Chem. Sci. 9 (2018) 7376-7389.

[23] Y.-X. Chen, Z.-H. Ge, M. Yin, D. Feng, X.-Q. Huang, W. Zhao, and J. He, Adv. Funct. Mater. 26 (2016) 6836-6845.

[24] X. Shi, A. Wu, T. Feng, K. Zheng, W. Liu, Q. Sun, M. Hong, S.T. Pantelides, Z.G. Chen, and J. Zou, Adv. Energy Mater. 9 (2019) 1803242.

[25] J.C. Li, D. Li, X.Y. Qin, and J. Zhang, Scripta Mater. 126 (2017) 6-10.

[26] Y.-M. Han, J. Zhao, M. Zhou, X.-X. Jiang, H.-Q. Leng, and L.-F. Li, J. Mater. Chem. A 3 (2015) 4555-4559.

[27] Y. Zhu, J. Carrete, Q.-L. Meng, Z. Huang, N. Mingo, P. Jiang, and X. Bao, J. Mater. Chem. A 6 (2018) 7959-7966.

[28] D. Li, J. Li, X. Qin, J. Zhang, H. Xin, C. Song, and L. Wang, Energy 116 (2016) 861-866.

[29] Y. Li, F. Li, J. Dong, Z. Ge, F. Kang, J. He, H. Du, B. Li, and J.-F. Li, J. Mater. Chem. C 4 (2016) 2047-2055.

[30] S.R. Popuri, M. Pollet, R. Decourt, F.D. Morrison, N.S. Bennett, and J.W.G. Bos, J. Mater. Chem. C 4 (2016) 1685-1691.

[31] X. Shi, A. Wu, W. Liu, R. Moshwan, Y. Wang, Z.-G. Chen, and J. Zou, ACS Nano 12 (2018) 11417-11425.

[32] H. Ju, M. Kim, D. Park, and J. Kim, Chem. Mater. 29 (2017) 3228-3236.

[33] Y.K. Lee, Z. Luo, S.P. Cho, M.G. Kanatzidis, and I. Chung, Joule 3 (2019) 719-731.

[34] X.-L. Shi, X. Tao, J. Zou, and Z.-G. Chen, Adv. Sci. 7 (2020) 1902923.

[35] X.L. Shi, K. Zheng, W.D. Liu, Y. Wang, Y.Z. Yang, Z.G. Chen, and J. Zou, Adv. Energy Mater. 8 (2018) 1800775.

[36] Z.H. Ge, Y. Qiu, Y.X. Chen, X. Chong, J. Feng, Z.K. Liu, and J. He, Adv. Funct. Mater. 29 (2019) 1902893.

[37] J. Cha, C. Zhou, Y.K. Lee, S.-P. Cho, and I. Chung, ACS Appl. Mater. Interfaces 11 (2019) 21645-21654.

[38] C. Chang, Q. Tan, Y. Pei, Y. Xiao, X. Zhang, Y.-X. Chen, L. Zheng, S. Gong, J.-F. Li, and J. He, RSC Adv. 6 (2016) 98216-98220.

[39] S. Li, Y. Wang, C. Chen, X. Li, W. Xue, X. Wang, Z. Zhang, F. Cao, J. Sui, and X. Liu, Adv. Sci. 5 (2018) 1800598.

[40] P.-P. Shang, J. Dong, J. Pei, F.-H. Sun, Y. Pan, H. Tang, B.-P. Zhang, L.-D. Zhao, and J.-F. Li, Research 2019 (2019) 1-10.

[41] C. Chiritescu, D.G. Cahill, N. Nguyen, D. Johnson, A. Bodapati, P. Keblinski, and P. Zschack, Science 315 (2007) 351.

[42] Q. Cheng, J. Pang, D. Sun, J. Wang, S. Zhang, F. Liu, Y. Chen, R. Yang, N. Liang, X. Lu, Y. Ji, J. Wang, C. Zhang, Y. Sang, H. Liu, and W. Zhou, InfoMat 2 (2020) 656-697.

[43] S. Yang, Y. Liu, M. Wu, L.-D. Zhao, Z. Lin, H.-c. Cheng, Y. Wang, C. Jiang, S.-H. Wei, L. Huang, Y. Huang, and X. Duan, Nano Res. 11 (2018) 554-564.

[44] J. Hong and O. Delaire, Mater. Today Phys. 10 (2019) 100093.

[45] G. Kresse and D. Joubert, Phys. Rev. B 59 (1999) 1758.

[46] J.P. Perdew, K. Burke, and M. Ernzerhof, Phys. Rev. Lett. 77 (1996) 3865.

[47] J.P. Perdew, J.A. Chevary, S.H. Vosko, K.A. Jackson, M.R. Pederson, D.J. Singh, and C. Fiolhais, Phys. Rev. B 46 (1992) 6671.

[48] H.J. Monkhorst and J.D. Pack, Phys. Rev. B 13 (1976) 5188.

[49] Q. Zhang, E.K. Chere, J. Sun, F. Cao, K. Dahal, S. Chen, G. Chen, and Z. Ren, Adv. Energy Mater. 5 (2015) 1500360.

[50] X. Wang, J. Xu, G. Liu, Y. Fu, Z. Liu, X. Tan, H. Shao, H. Jiang, T. Tan, and J. Jiang, Appl. Phys. Lett. 108 (2016) 083902.

[51] D. Li, X. Tan, J. Xu, G. Liu, M. Jin, H. Shao, H. Huang, J. Zhang, and J. Jiang, RSC Adv. 7 (2017) 17906-17912.

[52] F. Li, W. Wang, X. Qiu, Z.-h. Zheng, P. Fan, J.-t. Luo, and B. Li, Inorg. Chem. Front. 4 (2017) 1721-1729.

[53] M. Zhang, D. Wang, C. Chang, T. Lin, K. Wang, and L.-D. Zhao, J. Mater. Chem. C 7 (2019) 10507-10513.

[54] C.F. Wu, T.R. Wei, and J.F. Li, Phys. Chem. Chem. Phys. 17 (2015) 13006-13012.

[55] X. Li, C. Chen, W. Xue, S. Li, F. Cao, Y. Chen, J. He, J. Sui, X. Liu, and Y. Wang, Inorg. Chem. 57 (2018) 13800-13808.

[56] V.Q. Nguyen, T.H. Nguyen, J.E. Lee, S.-D. Park, J.Y. Song, H.-M. Park, A.T. Duong, and S. Cho, Nanoscale Res. Lett. 13 (2018) 200.

[57] S. Chen, K. Cai, and W. Zhao, Physica. B 407 (2012) 4154-4159.

[58] Q. Li, L. Zhang, J. Yin, Z. Sheng, X. Chu, F. Wang, and F. Zhu, J. Alloys Compd. 745 (2018) 513-518.

[59] J. Gainza, F. Serrano-Sánchez, M. Gharsallah, F. Carrascoso, J. Bermúdez, O.J. Dura, F.J. Mompean, N. Biskup, J.J. Meléndez, J.L. Martínez, J.A. Alonso, and N.M. Nemes, J. Appl. Phys. 126 (2019) 045105.

[60] H. Ju and J. Kim, Ceram. Int. 42 (2016) 9550-9556.

[61] Y. Shu, X. Su, H. Xie, G. Zheng, W. Liu, Y. Yan, T. Luo, X. Yang, D. Yang, and C. Uher, ACS Appl. Mater. Interfaces 10 (2018) 15793-15802.

Highlights

- A high *ZT* of ~1.35 is achieved in *n*-type polycrystalline SnSe at 790 K, ranking as a top value;
- Both experimental and DFT results confirm Pb/I co-doping in SnSe, making the system *n*-type;
- 2D WSe_2 nanoinclusions induce high-density WSe_2/SnSe interfaces, acting as energy barriers;
- Full-frequency phonon scattering is realized to significantly reduce the lattice thermal conductivity.

Graphical Abstract

ToC

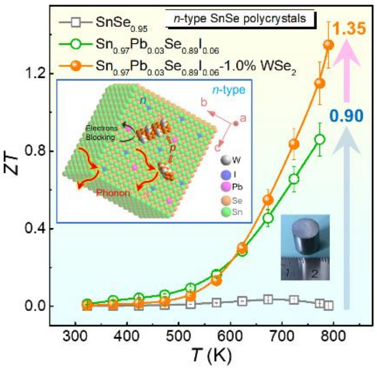

Two-Dimensional WSe_2/SnSe p-n Junctions Secure Ultrahigh Thermoelectric Performance in n-type Pb/I Co-doped Polycrystalline SnSe

Yue-Xing Chen [1,†], *Xiao-Lei Shi* [2,3,†], *Zhuang-Hao Zheng* [1,†,*], *Fu Li* [1], *Wei-Di Liu* [3], *Wen-Yi Chen* [3], *Xin-Ru Li* [1], *Guang-Xing Liang* [1], *Jing-Ting Luo* [1], *Ping Fan* [1,*], *Zhi-Gang Chen* [2,3,*]

[1] Shenzhen Key Laboratory of Advanced Thin Films and Applications, Key Laboratory of Optoelectronic Devices and Systems of Ministry of Education and Guangdong Province, College of Physics and Optoelectronic Engineering, Shenzhen University, Shenzhen 518060, P. R. China;

[2] Centre for Future Materials, University of Southern Queensland, Springfield Central, Brisbane, Queensland 4300, Australia;

[3] School of Mechanical and Mining Engineering, The University of Queensland, St Lucia, Brisbane, Queensland 4072, Australia.

† These authors contribute equally to this work.

* Corresponding authors:

Zhuang-Hao Zheng: zhengzh@szu.edu.cn;

Ping Fan: fangp@szu.edu.cn;

Zhi-Gang Chen: zhigang.chen@usq.edu.au, zhigang.chen@uq.edu.au.

Abstract:

In this study, we, for the first time, introduce p-type two-dimensional (2D) WSe_2 nanoinclusions in n-type Pb/I co-doped SnSe matrix to form WSe_2/SnSe p-n junctions. These p-n junctions act as energy barriers and effective phonon scattering sources, leading to a high figure-of-merit (*ZT*) of ~1.35 at ~790 K in n-type polycrystalline SnSe. First-principles density functional theory calculation results indicates that I-doping shifts Fermi level up into conduction bands of SnSe, making the system n-type behavior, while both Pb and I dopants act as point-defect-based short-wavelength phonon scattering centers. The introduced p-type 2D WSe_2 nanoinclusions induce high-density WSe_2/SnSe interfaces that act as p-n junctions, which block the electron carriers and rationally tune the carrier density, contributing to a high absolute Seebeck coefficient of ~470.7 $\mu V\ K^{-1}$ and a high power factor of ~5.9 $\mu W\ cm^{-1}\ K^{-2}$. Meanwhile, the dense phase boundaries and considerable lattice strains by the introduced 2D WSe_2 nanoinclusions significantly strengthen the mid- and long-wavelength phonon scattering, giving rise to a much low thermal conductivity of 0.35 $W\ m^{-1}\ K^{-1}$ and in turn a high *ZT* of ~1.35. This study provides a new strategy to achieve high thermoelectric performance in n-type polycrystalline SnSe.

Keywords: thermoelectric; SnSe; n-type; p-n junction; doping.

1. Introduction

Owing to the capability for direct energy conversion between heat and electricity, thermoelectric materials have been attracted significant attentions with full potentials for solving the issues of fossil fuel depletion and environmental pollutions by waste-heat recovery [1, 2]. The energy conversion efficiency of thermoelectric materials is evaluated by the dimensionless figure-of-merit ZT, defined as $ZT = S^2\sigma T/\kappa = S^2\sigma T/(\kappa_e + \kappa_l)$ [3], where σ is the electric conductivity, S is the Seebeck coefficient, $S^2\sigma$ is the power factor, T is the absolute temperature, κ is the total thermal conductivity, κ_e is the electronic thermal conductivity, and κ_l is the lattice thermal conductivity. In general, a high $S^2\sigma$ and a low κ are both required to achieve a high ZT value [4, 5]. To date, many thermoelectric materials have exhibited excellent thermoelectric performance with ZT values >2 by rational thermoelectric designs, such as $AgSbTe_2$ (ZT = ~2.1 at 573 K by Se-doping) [6], PbTe (ZT = ~2.51 at 823 K by doping with Na, Eu, and Sn) [7], GeTe (ZT = ~2.4 at 600 K by doping with Pb and Bi) [8], liquid-like $Cu_{2-x}Se$ (ZT = ~2.62 at 1029 K by 2 % Al-doping) [9, 10], and SnSe crystals (ZT = ~2.8 at 773 K by Br-doping) [11].

Among these state-of-the-art thermoelectric materials, SnSe-based bulk materials have drawn considerable attention due to their suitable bandgap (~0.9 eV) [3], cost-effectiveness [12], and low-toxic feature [13], making them good candidates with great potentials for applications in low-cost thermoelectric devices [14, 15]. Especially, n-type SnSe single crystals were reported to exhibit a record-high ZT of ~2.8 at 773 K [11], owing to their high $S^2\sigma$ and remarkably low κ. However, the undesirable mechanical properties make the single crystals easy to cleave along the *b*- or *c*-directions [12], and the issues of high-cost and time-consuming in the production of SnSe single crystals severely limit their applications in thermoelectric devices at an industrial scale [11, 12, 16]. Therefore, mechanically robust and low-cost polycrystalline SnSe becomes a promising alternative candidate, and has gained significant attention in recent years.

Because pristine polycrystalline SnSe possess a relatively low $S^2\sigma$ and high κ [17], many strategies have been employed to improve their thermoelectric performance [18], such as vacancy engineering [19-21], doping [22-25], multi-phase alloying [26-28], anisotropy strengthening [29, 30], and nanoporosity design [31, 32]. The peak ZT values have been improved from ~0.5 to ~2.5 for p-type polycrystalline SnSe [3, 18, 33, 34]. However, it is still challenging with only few works to achieve a high ZT of >1.0 in the n-type polycrystalline SnSe due to the p-type nature of pristine SnSe [35-40], and the mechanisms for the n-type thermoelectric behaviors in SnSe are still unclear. Moreover, developing high-performance n-type SnSe-based polycrystalline is urgent because same material systems are the best for the assembly of thermoelectric devices due to their similar thermodynamics, mechanical and welding properties.

I^- can release extra electrons into the system when substituting Se-sites (Se^{2-}) in SnSe, realizing n-type doping. By controlling the I-doping level, a well-tuned electron concentration can be achieved to optimize $S^2\sigma$. In addition, because Pb^{2+} possesses a much larger ionic radius of 1.20 Å than Sn^{2+} (0.93 Å) while I^- also possesses a larger ionic radius of 2.16 Å than Se^{2-} (1.84 Å), both Pb and I can act as point-defect-based phonon scattering centers to reduce κ (κ_l) by strengthening the short-wavelength phonon scattering. Based on Pb/I co-doping, to further realize high $S^2\sigma$ and low κ_l, one of the most effective strategies is introducing suitable nanoinclusions in the SnSe matrix [3]. The nanoinclusions should possess low dimensions to provide more phase boundaries as energy barriers to filter or block carriers and in turn improve S, and act as phonon scattering sources to strengthen the phonon scattering and in turn reduce κ_l. To realize this objective, we found p-type two-dimensional (2D) WSe_2 nanoinclusions are good candidates. WSe_2 possesses a high melting point of >1473 K [41], which is much higher than that of SnSe (1134 K) [3], therefore WSe_2 can be well maintained in SnSe matrix. WSe_2 is a typical p-type semiconductor that possesses a typical bandgap of ~1.5 eV and a unique 2D crystal structure [42], which can form high-density WSe_2-SnSe interfaces with the n-type SnSe phase, acting as p-n junctions. Such a strong energy barrier can block the electron carriers and rationally tune the carrier density, contribute to a high *S*. Besides, 2D WSe_2 was pointed out to has an ultralow intrinsic κ of only 0.05 W m^{-1} K^{-1} [41]. In addition, the introducing of 2D WSe_2 nanoinclusions provides extra phonon scattering sources in the polycrystals, including the high-density phase boundaries that target to scatter the long-wavelength phonons, and significant strain fields in the surrounding SnSe lattices. Therefore, we combine Pb/I co-doping that enable an n-type thermoelectric behavior and introduce 2D WSe_2 nanoinclusions to achieve high-performance n-type polycrystalline SnSe, as illustrated in **Figure 1(a)**.

2. Experimental Details

Fabrication. n-type polycrystalline SnSe pellets were fabricated by a combination of solid-state reaction and sparkle plasma sintering (SPS) technique. High-purity Sn chunk (99.99 %), Se chunk (99.99 %), PbI_2 powders (99.99 %), and WSe_2 nanopowders (99.9 %) were weighed as precursors, in which PbI_2 acted as dopant sources, and WSe_2 nanopowders acted as nanoinclusions. To reduce the native Sn vacancy concentration in pristine SnSe for promoting the n-type doping, the ratio of Se to Sn was set as 0.95:1, described as $SnSe_{0.95}$ (nominal composition). Two sets of compositions, namely $Sn_{1-x}Se_{0.95-2x}(PbI_2)_x$ (x = 0, 0.01, 0.03, and 0.05) and $Sn_{0.97}Pb_{0.03}Se_{0.89}I_{0.06}$-$y$ % WSe_2 (y = 0.5, 1.0, 2.0, and 4.0), were determined. The mixed precursors were loaded and sealed into evacuated quartz tubes with a pressure of $<10^{-4}$ Pa, and carefully sealed. The quartz tubes were placed in a box furnace and heated up to 1223 K with a heating rate of 100 K h^{-1}, soaking for 24 h. The tubes were slowly cooling down and broken. The obtained ingots were ground into powders by mortar-pestle and consolidated by using a SPS system (LABOX-325, Japan) at 773 K for 5 min under the pressure of 50 MPa. The sintered pellets were cylindric with dimensions of Φ10 mm × 12 mm, as shown in **Figure 1(b)** (top).

Characterization. For our fabricated n-type polycrystalline SnSe, the phases were confirmed by X-ray diffraction (XRD, CuKα, Riguku, Japan), the morphologies were investigated by field emission scanning electron microscopy (FE-SEM, Zeiss Merlin, Germany), the nanostructures were studied by spherical aberration-corrected (Cs-corrected) scanning transmission electron microscopy (STEM, Titan Cubed Themis G2 300, FEI, USA), and the real compositions were determined by electron probe micro-analyzer (EPMA, JXA8230, JEOL) and energy dispersive spectrometer (EDS) embedded in the FE-SEM and Cs-corrected STEM.

Performance. Polycrystalline SnSe is a typical anisotropy material due to its 2D orthorhombic crystal structure with strong anharmonic bonding [43, 44]. To evaluate the thermoelectric performance of our fabricated n-type polycrystalline SnSe, the pellets were cut into small pieces to measure the properties along the direction perpendicular (abbreviated as ⊥) and parallel (abbreviated as //) to the sintering pressure, as illustrated in **Figure 1(b)** (bottom). S and σ were measured from 300 to 790 K using an Ulvac-Riko ZEM-3 instrument in a thin helium atmosphere. κ was calculated using the relationship of $\kappa = D\rho C_p$ [19], in which the density ρ was measured using the Archimedes method [19], as shown in **Table S1**, and thermal diffusivity D was measured using laser flash equipment (NETZSCH Laser Flash Apparatus LFA 457, Germany). Specific heat C_p were taken from the literature [11]. The carrier concentrations n were derived from the formula $n = 1/eR_\mathrm{H}$, where e is the electronic charge, and R_H is the Hall coefficient. R_H was measured by the Van der Pauw method using a Hall measurement system (Lake Shore 8400 Series, Model 8404, USA) under a reversible magnetic field (0.8 T) in a wide temperature range from 300 to 773 K. The carrier mobility μ was calculated by $\mu = \sigma R_\mathrm{H}$. In terms of the determination of error bars, the combined uncertainty for the experimental determination of ZT is about 15%–20% and is caused by the five respective measurement including σ, S, D, and ρ.

Calculation. The calculations in this work were based on first-principles density functional theory (DFT). The structural relaxations and electronic structures were carried out using the projector augmented wave (PAW) method as implemented in the VASP code [45], and the exchange-correlation functional was approximated using the generalized gradient approximation (GGA) [46] with Perdew-Burke-Ernzerhof (PBE) parametrization [47]. The cut-off energy of the plane-wave was set to be 500 eV to ensure convergence. The convergence criteria of the force and the energy were 1×10^{-3} eV Å^{-1} and 1×10^{-7} eV, respectively. The 2D Brillouin zone integration was done with a ***k***-mesh density of 100/*a* [48]. The doping SnSe systems were constructed by a 2 × 2 ×2 (64 atoms) supercell.

3. Results and Discussions

In order to optimize the thermoelectric performance of our n-type polycrystalline SnSe pellets, the best concentrations of Pb, I, and 2D WSe_2 nanoinclusions are firstly explored. Two sets of compositions, namely $Sn_{1-x}Pb_xSe_{0.95-2x}I_{2x}$ ($x = 0$, 0.01, 0.03, and 0.05) and $Sn_{0.97}Pb_{0.03}Se_{0.89}I_{0.06}$-$y$ % WSe_2 ($y = 0.5$, 1.0, 2.0, and 4.0), were determined. **Figure 1(c)** compares the temperature-dependent *ZT* of our fabricated n-type polycrystalline SnSe pellets doped with different content of Pb, I, and 2D WSe_2 nanoinclusions, in which a promising *ZT* of ~0.9 at 773 K can be achieved by co-doping with 3 % Pb and 6 % I ($x = 0.03$), and a high *ZT* of ~1.35 at 790 K can be further achieved by introducing 1 % 2D WSe_2 nanoinclusion ($y = 1.0$). Such an outstanding thermoelectric performance possesses full potentials for applying in thermoelectric devices as n-type “legs” for the high-temperature power generation.

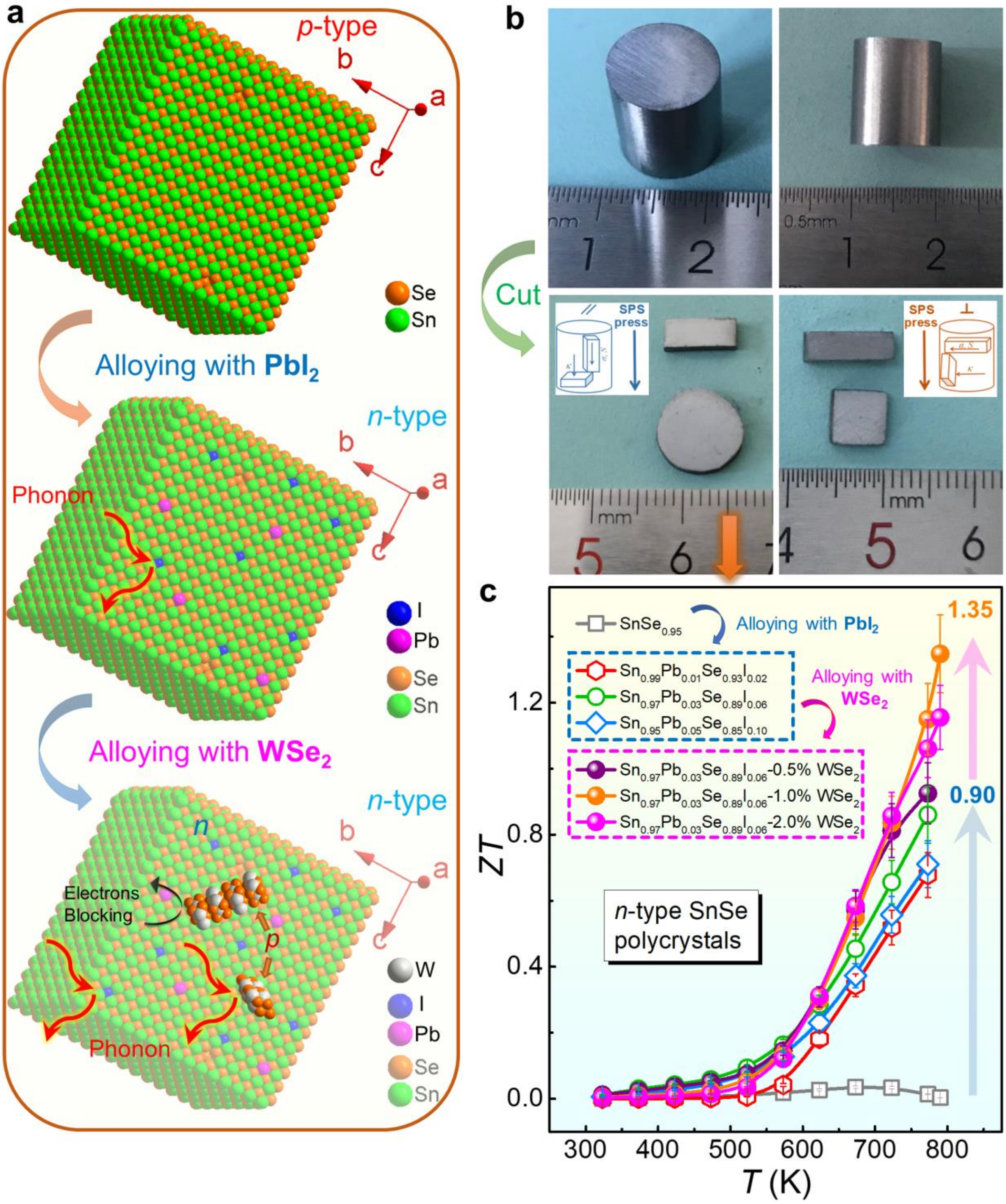

Figure 1. (a) Schematic diagrams of the strategies for boosting the thermoelectric performance of n-type polycrystalline SnSe, including Pb/I co-doping and alloying with WSe_2 nanoinclusions. (b) Optical images of the n-type polycrystalline SnSe pellets doped with 3 % Pb and 6 % I and alloyed with 1 % WSe_2 nanoinclusions (top). The bulk samples are cut for evaluating their thermoelectric performance along the direction parallel (//, bottom-left) and perpendicular (▯, bottom-right) to the sintering pressure. (c) Temperature-dependent *ZT* of n-

type polycrystalline SnSe pellets doped with different content of Pb, I, and WSe_2 nanoinclusions.

Because the real compositions may be slightly different from the nominal compositions during the solid-state reaction and SPS processing, we determined the real compositions of our fabricated $Sn_{1-x}Pb_xSe_{0.95-2x}I_{2x}$ pellets by using EPMA, and the results are listed in **Table 1**. As can be seen, the solubility of I should be ~0.5 % since the real I contents for $x = 0.03$ and 0.05 are almost the same, while the Pb has not reached its upper limit of solubility in SnSe.

Table 1. Comparison of nominal and real compositions of the as-fabricated $Sn_{1-x}Pb_xSe_{0.95-2x}I_{2x}$ bulk samples.

***x* value**	**Nominal composition**	**Real composition**	**Sn (at%)**	**Se (at%)**	**Pb (at%)**	**I (at%)**
0	$SnSe_{0.95}$	SnSe	50.01	49.99	0	0
0.01	$Sn_{0.99}Pb_{0.01}Se_{0.93}I_{0.02}$	$Sn_{0.989}Pb_{0.011}Se_{0.962}I_{0.001}$	50.37	48.99	0.56	0.08
0.03	$Sn_{0.97}Pb_{0.03}Se_{0.89}I_{0.06}$	$Sn_{0.974}Pb_{0.026}Se_{0.957}I_{0.005}$	49.66	48.77	1.32	0.25
0.05	$Sn_{0.95}Pb_{0.05}Se_{0.85}I_{0.10}$	$Sn_{0.958}Pb_{0.042}Se_{0.954}I_{0.005}$	48.92	48.68	2.14	0.26

Figure 2(a) shows XRD patterns of $Sn_{1-x}Pb_xSe_{0.95-2x}I_{2x}$ ($x = 0$, 0.01, 0.03, and 0.05) along the // direction in a 2θ range from 20° to 70°. All the peaks can be indexed as α-SnSe with a space group of *Pnma* (PDF#48-1224) [20], and no impurity phase can be observed within the detection limit of the XRD spectrometer, indicating all samples have a single SnSe phase with an orthorhombic crystal structure and lattice parameters of $a = 11.37$ Å, $b = 4.19$ Å, and $c = 4.44$ Å. The strongest peak corresponds to the (111) plane, which is different from the XRD results along the ⍰ direction (refer to **Figure S1(a)** in the Supporting Information that the (400) is the strongest peak), indicating the anisotropy of polycrystalline SnSe. The magnified XRD patterns of (111) peaks are shown in **Figure 2(b)**. As can be seen, the peaks of the doped samples slightly shift toward a small angle, suggesting an expansion of the crystal cell. Because Pb^{2+} has a much larger ionic radius of 1.20 Å than Sn^{2+} (0.93 Å) while I^- possesses a larger ionic radius of 2.16 Å than Se^{2-} (1.84 Å), such an expansion in the crystal cell is reasonable, confirming the successful doping of Pb and I. In addition, a similar left-shift of (400) peaks can also be observed in the XRD patterns along the ⍰ direction (refer to **Figure S1(b)**), double confirming the expansion of the crystal cell by Pb and I co-doping.

Figure 2(c) shows a FE-SEM image of $Sn_{0.97}Pb_{0.03}Se_{0.89}I_{0.06}$ pellet fractured along the // direction ($x = 0.03$). The fractured surface shows a typical layered morphology, which explains the anisotropy observed in XRD patterns. SEM images of pellets along the // direction for $x = 0$, 0.01 and 0.05 are shown in **Figure S2(a-c)**, and SEM image of pellet ($x = 0.05$) along the ⍰ direction can be referred to **Figure S2(d)**. **Figure 2(d)** shows a Cs-corrected STEM high-angle annular dark-field (HAADF) image of $Sn_{0.97}Pb_{0.03}Se_{0.89}I_{0.06}$, from which grain boundaries can be clearly observed. **Figure 2(e)** shows corresponding EDS maps for Sn, Se, Pb, and I, confirming the homogeneous doping of both Pb and I at a microscale. EDS maps based on SEM back-scattered electron (BSE) image taken from the polished surface of $Sn_{0.97}Pb_{0.03}Se_{0.89}I_{0.06}$ pellet can be referred to **Figure S3**, double confirming the homogeneous distribution of Sn, Se, Pb, and I. **Figure 2(f)** is a high-resolution Cs-corrected STEM-HAADF image of $Sn_{0.97}Pb_{0.03}Se_{0.89}I_{0.06}$, in which a typical grain boundary is clearly seen. Some lattice contrast can be seen in the grains, which may be caused by the doping of Pb and I. **Figure 2(g)** shows a high-resolution transmission electron microscopy (HRTEM) image of $Sn_{0.97}Pb_{0.03}Se_{0.89}I_{0.06}$, in which a typical lattice contrast can be observed. The insets show the corresponding fast Fourier transform (FFT) pattern (top-right) and an intensity line profile (bottom-right) taken from the pink dashed line. The FFT pattern indicates that the lattice is viewed along the [001] direction, confirming the crystal nature of SnSe; while the intensity line profile confirms the lattice contrast that caused by the Pb/I co-doping. **Figure 2(h)** shows a high-resolution Cs-corrected STEM-HAADF image of $Sn_{0.97}Pb_{0.03}Se_{0.89}I_{0.06}$, in which the lattice contrasts can be clearer observed as indicated by the arrows. These results confirm that Pb and I were successfully doped into the SnSe lattice.

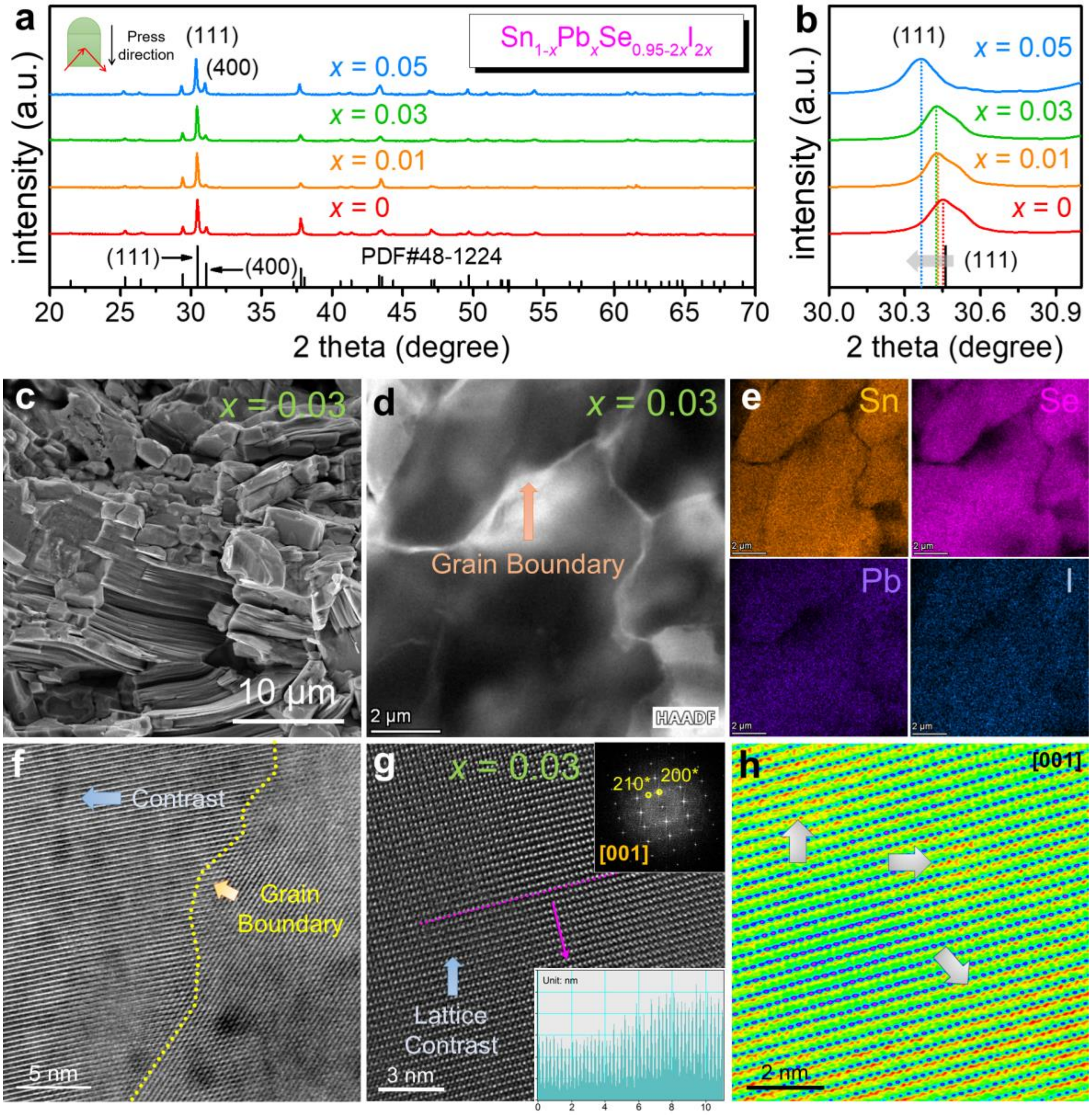

Figure 2. (a) X-ray diffraction (XRD) patterns of $Sn_{1-x}Pb_xSe_{0.95-2x}I_{2x}$ ($x = 0, 0.01, 0.03$, and 0.05) along the // direction in a 2θ range from 20° to 70°. (b) Magnified XRD patterns of (111) peaks. (c) Field emission scanning electron microscopy (FE-SEM) images of $Sn_{0.97}Pb_{0.03}Se_{0.89}I_{0.06}$ along the // direction ($x = 0.03$). (d) Spherical aberration-corrected (Cs-corrected) scanning transmission electron microscopy (STEM) high-angle annular dark-field (HAADF) image of $Sn_{0.97}Pb_{0.03}Se_{0.89}I_{0.06}$. (e) Corresponding energy dispersive spectrometer (EDS) maps for Sn, Se, Pb, and I. (f) High-resolution Cs-corrected STEM-HAADF image of $Sn_{0.97}Pb_{0.03}Se_{0.89}I_{0.06}$ showing a typical grain boundary. (g) High-resolution transmission electron microscopy (HRTEM) image of $Sn_{0.97}Pb_{0.03}Se_{0.89}I_{0.06}$ showing a typical lattice contrast. The insets show the corresponding fast Fourier transform (FFT) pattern (top-right) and an intensity line profile

(bottom-right) taken from the pink dashed line. (h) High-resolution Cs-corrected STEM-HAADF image of $Sn_{0.97}Pb_{0.03}Se_{0.89}I_{0.06}$ showing typical lattice contrasts indicated by arrows.

Figure 3(a) compares temperature-dependent S of $Sn_{1-x}Pb_xSe_{0.95-2x}I_{2x}$ (x is 0, 0.01, 0.03, and 0.05), measured along the // direction. It is clearly seen that after doping with Pb and I, n-type SnSe is successfully realized. A high absolute S value of ~429.0 μV K^{-1} at 773 K can be seen when $x = 0.01$. **Figure 3(b)** shows temperature-dependent σ of $Sn_{1-x}Pb_xSe_{0.95-2x}I_{2x}$ (x is 0, 0.01, 0.03, and 0.05). With increasing the doping concentration of Pb and I, σ is significantly enhanced, mainly derived from the extra electron carriers provided by the I^- that substitute Se-sites. **Figure 3(c)** shows the determined $S^2\sigma$ of $Sn_{1-x}Pb_xSe_{0.95-2x}I_{2x}$ (x is 0, 0.01, 0.03, and 0.05). An optimized $S^2\sigma$ of ~5.1 μW cm^{-1} K^{-2} at 773 K can be observed when $x = 0.03$, derived from the coupling of S and σ. **Figure 3(d)** shows x-dependent n and μ of $Sn_{1-x}Pb_xSe_{0.95-2x}I_{2x}$ (x is 0, 0.01, 0.03, and 0.05). With increasing the doping concentration of Pb and I, n is significantly enhanced, while μ is first decreased due to the p-n transition from $x = 0$ to $x = 0.01$, and then increased due to the increase of n. **Figure 3(e)** shows calculated effective mass m^* and deformation potential E_{def} of $Sn_{1-x}Pb_xSe_{0.95-2x}I_{2x}$ as a function of x value. As can be seen, with increasing the x until $x = 0.03$, m^* reaches to the maximized value while E_{def} reach to the minimized value in our samples, indicating that a couple of S and σ has been realized, leading to an optimized $S^2\sigma$. **Figure 3(f)** compares temperature-dependent κ of $Sn_{1-x}Pb_xSe_{0.95-2x}I_{2x}$ (x is 0, 0.01, 0.03, and 0.05) measured along the // direction. A low κ of ~0.43 W m^{-1} K^{-1} at 773 K can be observed when $x = 0.01$, indicating a significant reduction of κ compared with pristine SnSe (κ of 0.54 W m^{-1} K^{-1}). **Figure 3(g)** shows determined temperature-dependent κ_l of $Sn_{1-x}Pb_xSe_{0.95-2x}I_{2x}$ (x is 0, 0.01, 0.03, and 0.05). The achieved κ_l is close to the corresponding κ, indicating that κ_l dominates κ. The reduction of κ_l can be attributed to the Pb and I co-doping, since both Pb and I act as point-defect-based phonon scattering centers to strengthen the short-wavelength phonon scattering. The calculated temperature-dependent Lorenz number L and κ_e

are shown in **Figure S4**. **Figure 3(h)** shows 1000/T-dependent κ_l of $Sn_{1-x}Pb_xSe_{0.95-2x}I_{2x}$ (x is 0, 0.01, 0.03, and 0.05). It is clearly seen that all the plots show a linear relationship, indicating that the Umklapp phonon scattering dominates the phonon scattering [19, 22, 24, 35]. **Figure 3(i)** compares determined temperature-dependent ZT of $Sn_{1-x}Pb_xSe_{0.95-2x}I_{2x}$ (x is 0, 0.01, 0.03, and 0.05). A promising ZT of 0.9 at 773 K can be achieved by co-doping with 3 % Pb and 6 % I ($x = 0.03$), indicating that Pb and I co-doping benefit the high thermoelectric performance of n-type SnSe. The thermoelectric performance of $Sn_{1-x}Pb_xSe_{0.95-2x}I_{2x}$ measured or determined along the ⍰ direction can be referred to **Figure S5** in the supporting information. A peak ZT of ~0.6 can be seen in $Sn_{0.97}Pb_{0.03}Se_{0.89}I_{0.06}$ ($x = 0.3$), which is lower than that achieved along the // direction. In addition, the real compositions for the Pb/I co-doped SnSe samples after electrical and thermal property test can be referred to **Table S2** in the supporting information, evaluated by EPMA, and the differential scanning calorimetry (DSC) test of the sample $Sn_{0.97}Pb_{0.03}Se_{0.89}I_{0.06}$ is also shown in **Figure S6(a)**. These results indicate that our samples possess high thermal stability.

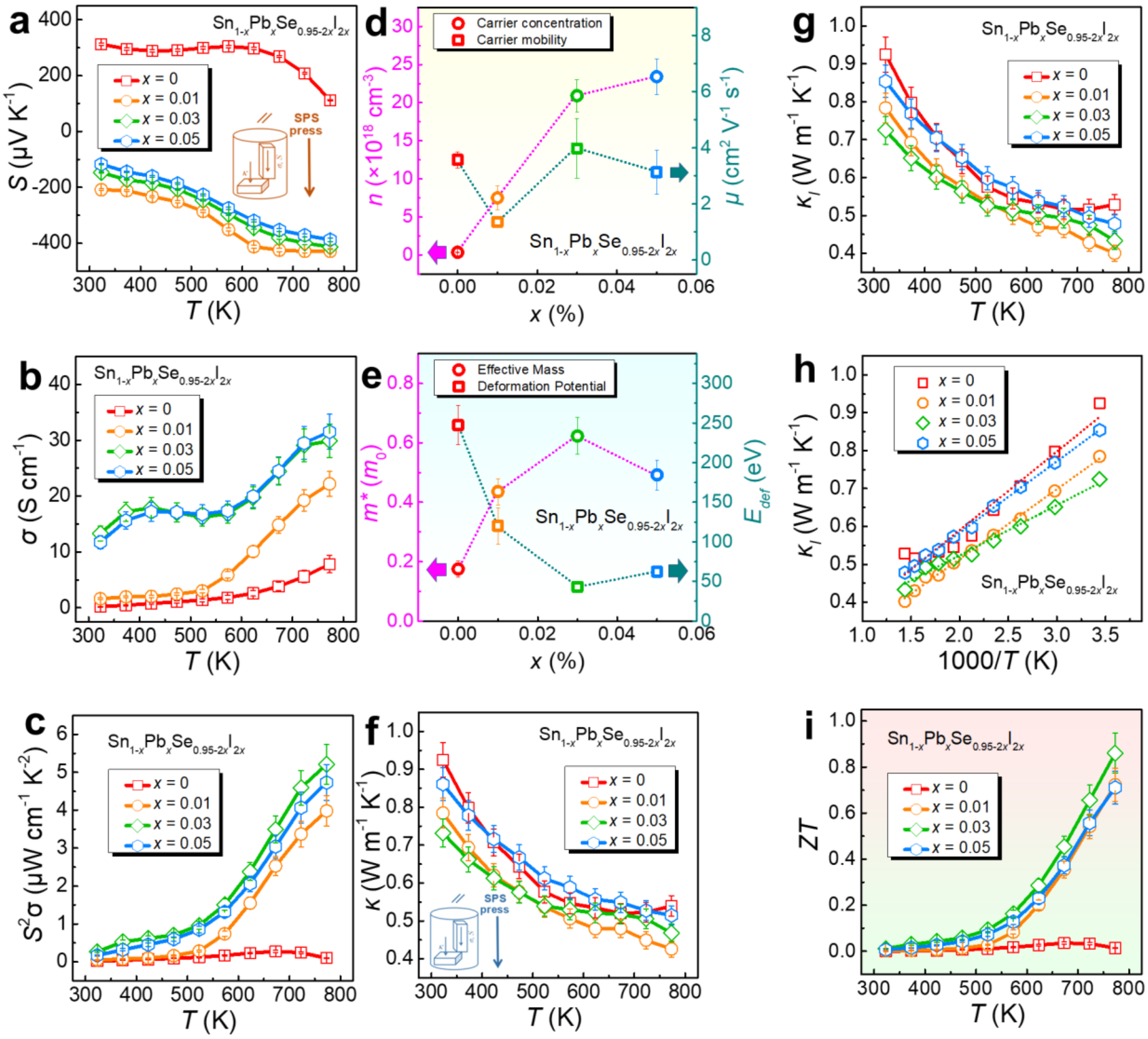

Figure 3. *T*-dependent (a) *S*, (b) *σ*, and (c) $S^2\sigma$ of $Sn_{1\text{-}x}Pb_xSe_{0.95\text{-}2x}I_{2x}$. *x*-dependent room-temperature (d) *n* and *μ*, and (e) *m** and E_{def} of $Sn_{1\text{-}x}Pb_xSe_{0.95\text{-}2x}I_{2x}$. *T*-dependent (f) *κ* and (g) κ_l of $Sn_{1\text{-}x}Pb_xSe_{0.95\text{-}2x}I_{2x}$. (h) 1000/*T*-dependent κ_l of $Sn_{1\text{-}x}Pb_xSe_{0.95\text{-}2x}I_{2x}$, and (i) *T*-dependent *ZT* of $Sn_{1\text{-}x}Pb_xSe_{0.95\text{-}2x}I_{2x}$. Here *x* is 0, 0.01, 0.03, and 0.05, respectively. All properties are measured or determined along the // direction.

To illustrate the mechanism of the increased *n* and *σ* by Pb/I co-doping, we performed DFT calculations on the electronic band structures for SnSe before and after Pb-doping, I-doping, and Pb/I co-doping. **Figure 4(a-d)** show calculated band structures of pristine, Pb-doped, I-doped, and Pb/I co-doped SnSe, respectively, and **Figure 4(e-h)** show their corresponding DOS. Interestingly, before and after Pb^{2+} replacing Sn^{2+}, the band structures and DOS are almost identical with the only difference being that the bands in the pristine SnSe lattice slightly split after Pb atoms are introduced. In contrast, after I^- replacing Se^{2-}, Fermi level moves into the conduction band, making the material n-type with significantly increased electron concentration. Therefore, it can be concluded that I dopant can introduce more electrons in SnSe.

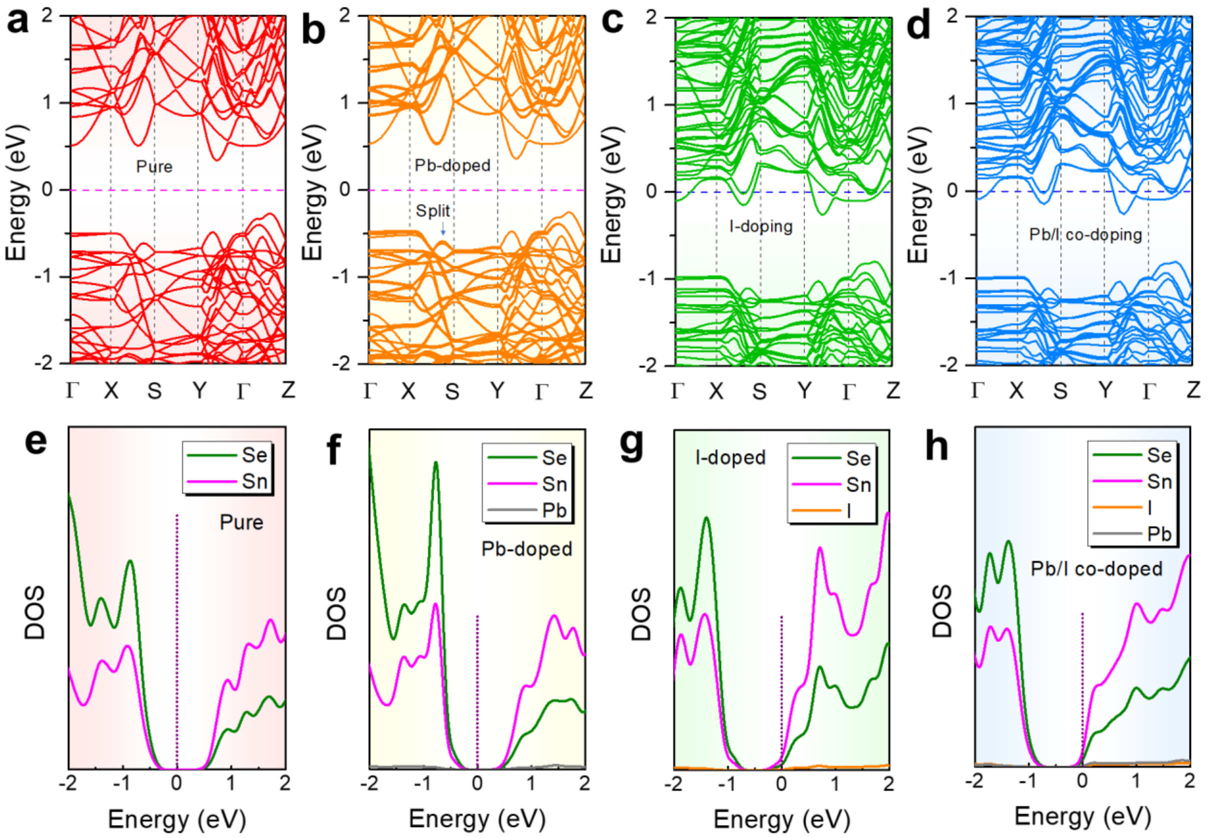

Figure 4. Calculated band structures of (a) pristine, (b) Pb-doped, (c) I-doped, and (d) Pb/I co-doped SnSe, and corresponding DOS of (e) pristine, (f) Pb-doped, (g) I-doped, and (h) Pb/I co-doped SnSe, respectively.

To further improve the thermoelectric performance of n-type polycrystalline SnSe, we introduce 2D WSe_2 nanoplates with an average size of ~393.8 nm (refer to **Figure S7**) as nanoinclusions in the $Sn_{0.97}Pb_{0.03}Se_{0.89}I_{0.06}$ matrix with different contents, described as $Sn_{0.97}Pb_{0.03}Se_{0.89}I_{0.06}$-$y$ % WSe_2 (y = 0, 0.5, 1.0, 2.0, and 4.0). Because WSe_2 has a much higher melting point of >1473 K than SnSe (1134 K) [3], WSe_2 nanoinclusions can be well maintained during solid-state reaction and SPS process. The DSC test of the sample $Sn_{0.97}Pb_{0.03}Se_{0.89}I_{0.06}$ + 1 % WSe_2 is shown in **Figure S6(b)**, indicating high thermal stability. **Figure 5(a)** shows XRD patterns of $Sn_{0.97}Pb_{0.03}Se_{0.89}I_{0.06}$-$y$ % WSe_2 along the // direction in a 2θ range from 10° to 60°. For the samples with $y < 4.0$, all the peaks can be indexed as α-SnSe with a space group of *Pnma* (PDF#48-1224) and lattice parameters of a = 11.37 Å, b = 4.19 Å, and c = 4.44 Å [20], and no obvious impurity phase can be observed within the detection limit of the XRD spectrometer. In contrast, WSe_2 nanophase can be detected only when $y = 4$, indicating the lower-content of WSe_2 nanoinclusions in SnSe may be out of the detection limit of the XRD spectrometer. The XRD patterns of $Sn_{0.97}Pb_{0.03}Se_{0.89}I_{0.06}$-$y$ % WSe_2 along the ⊥ direction can be referred to **Figure S8(a)**. **Figure 5(b)** shows FE-SEM image of $Sn_{0.97}Pb_{0.03}Se_{0.89}I_{0.06}$-1 % WSe_2 fractured along the // direction, from which typical layered morphology can be seen, similar to the samples before embedding WSe_2 nanoinclusions. However, it is still failed to observe the WSe_2 nanoinclusions under such a "large" scale by SEM, therefore TEM-based characterizations are needed. FE-SEM images of $Sn_{0.97}Pb_{0.03}Se_{0.89}I_{0.06}$-$y$ % WSe_2 for y = 0.5, 2.0, and 4.0 can be referred to **Figure S8(b-d)**. **Figure 5(c)** shows a Cs-corrected STEM-HAADF image of $Sn_{0.97}Pb_{0.03}Se_{0.89}I_{0.06}$-1 % WSe_2, from which a typical inclusion with different contrast from the surrounding area can be clearly seen. **Figure 5(d)** shows a Cs-corrected STEM-HAADF image magnified from **Figure 5(c)** (the square area). The inclusion has an irregular shape with a dimension of <300 nm, indicating a typical nanoinclusion. **Figure 5(e)** shows a high-resolution Cs-corrected STEM-HAADF image magnified from **Figure 5(d)** (the square area). Clearly, the lattice of the secondary phase is distinct from the dominant phase, and the dominant phase can be indexed as SnSe viewed along the [021] direction by the inset FFT pattern. There are also obvious lattice distortions found in the secondary phase. **Figure 5(f)** shows a high-resolution Cs-corrected STEM-HAADF image of SnSe phase viewed along the [021] direction, in which the overlays show Se or I atoms in blue and Sn or Pb atoms in yellow, all indicating the typical orthorhombic α-SnSe phase. **Figure 5(g-j)** show EDS maps on the interface for total elements, Sn, W, and Se, respectively. As shown in the contrast, the secondary nanophase can be indexed as WSe_2. The EDS results of $Sn_{0.97}Pb_{0.03}Se_{0.89}I_{0.06}$-2 % WSe_2 can be referred to **Figure S9**.

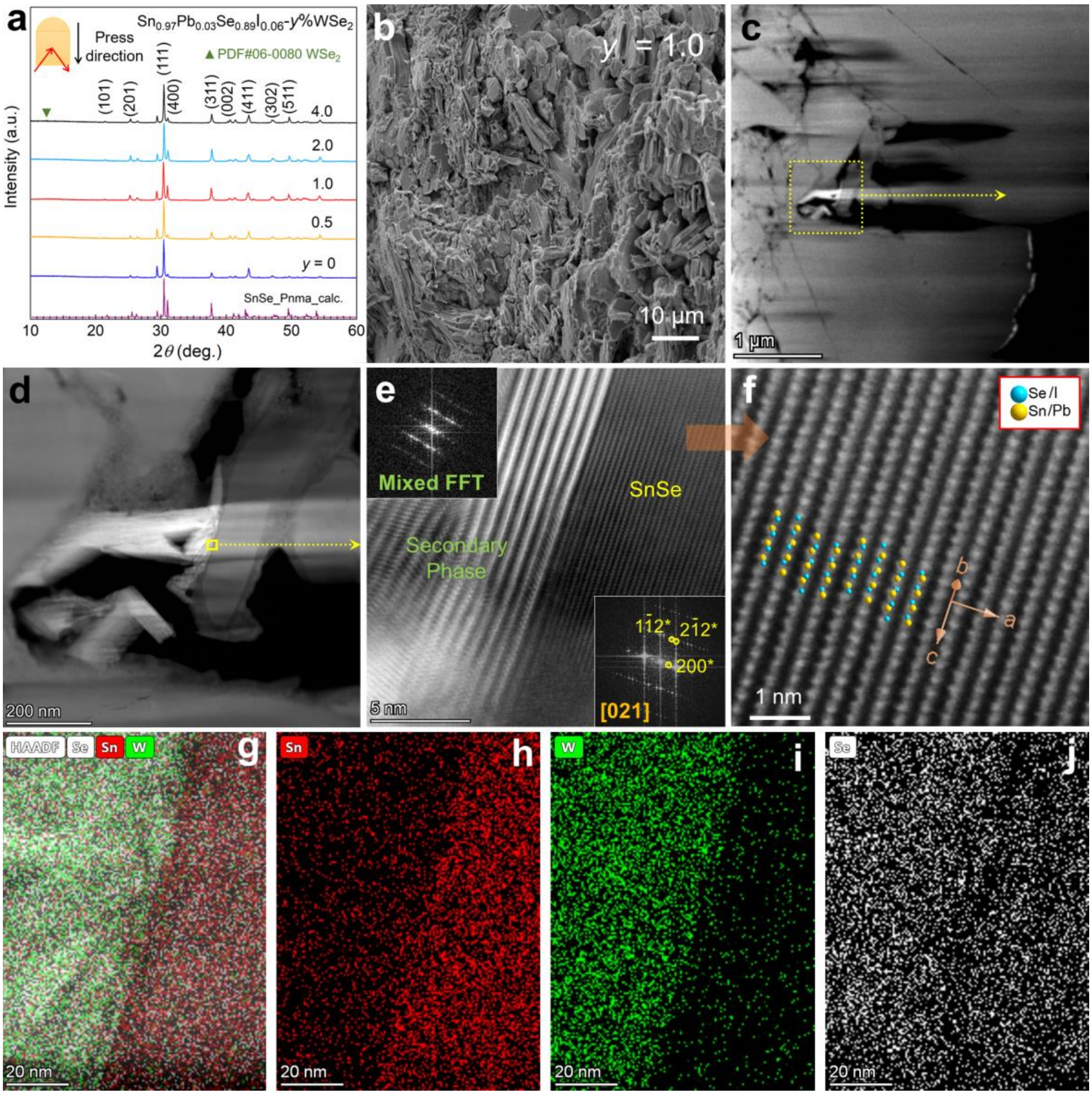

Figure 5. (a) XRD patterns of $Sn_{0.97}Pb_{0.03}Se_{0.89}I_{0.06}$-$y$ % WSe_2 (y = 0, 0.5, 1.0, 2.0, and 4.0) along the // direction in a 2θ range from 10° to 60°. (b) FE-SEM image of $Sn_{0.97}Pb_{0.03}Se_{0.89}I_{0.06}$-1 % WSe_2 along the // direction. (c) Cs-corrected STEM-HAADF image of $Sn_{0.97}Pb_{0.03}Se_{0.89}I_{0.06}$-1 % WSe_2. (d) Magnified Cs-corrected STEM-HAADF image taken from (c) to show the nanoinclusion. (e) Magnified high-resolution Cs-corrected STEM-HAADF image taken from (d) to show the interface between SnSe phase and the secondary phase. The SnSe phase can be indexed as viewed along the [021] direction, indicated by the inset FFT

pattern. (f) HR-STEM-HAADF image of the SnSe phase along the [021] direction, and EDS maps on the interface for (g) total, (h) Sn, (i) W, and (j) Se, respectively.

Figure 6(a-c) compares temperature-dependent S, σ, and $S^2\sigma$ of $Sn_{0.97}Pb_{0.03}Se_{0.89}I_{0.06}$-$y$ % WSe_2 (y = 0, 0.5, 1.0, and 2.0.) measured along the // direction. As can be seen, after introducing WSe_2 nanoinclusions, the absolute S is significantly enhanced, benefiting from the "depletion layer effect" driven by the p-n junction and potentially reduced n. A high absolute S value of ~470.7 μV K^{-1} at 790 K is observed when y = 1. With increasing the content of 2D WSe_2 nanoinclusions, σ is reduced. Considering that 2D WSe_2 nanoinclusions obviously increase the density of phase boundary, most of the low-energy carriers were scattered at these phase boundaries, leading to a lower σ. As a result, an optimized $S^2\sigma$ of ~5.9 μW cm^{-1} K^{-2} at 790 K can be observed when y = 1, derived from the coupling of S and σ. **Figure 6(d)** shows n and μ of $Sn_{0.97}Pb_{0.03}Se_{0.89}I_{0.06}$-$y$ % WSe_2 as a function of y value. With increasing the content of WSe_2 nanoinclusions, n is reduced, explaining the reduction of σ and the improvement of S; while μ is fluctuated. The introduction of p-type 2D WSe_2 nanoinclusions induces high-density WSe_2/SnSe interfaces that act as p-n junctions, which arises the "depletion layer effect" and leads to the decrease of n. **Figure 6(e)** shows calculated effective mass m^* and deformation potential E_{def} of $Sn_{0.97}Pb_{0.03}Se_{0.89}I_{0.06}$-$y$ % WSe_2 as a function of y value. It can be seen that with increasing the y, m^* is reduced, indicating an enhanced absolute S (for n-type); while E_{def} is increased, indicating the increase of μ. In fact, the calculated m^* and E_{def} for $Sn_{0.97}Pb_{0.03}Se_{0.89}I_{0.06}$-$y$ % WSe_2 can only be used for reference since the samples have more than one phase. **Figure 6(f)** illustrates the mechanism of depletion layer effect by WSe_2/SnSe phase boundaries that act as p-n junctions, in which the bandgap value of p-type WSe_2 (0.87 eV) comes from the calculated band structure of WSe_2 (refer to **Figure S10**), and the bandgap value of n-type SnSe (0.59 eV) comes from the calculated band structure of Pb/I co-doped SnSe (refer to **Figure 4**). The p-n junctions result in build-in electric fields around the phase boundaries, which are responsible for the fluctuation of μ. In addition, the band alignment at the interface between the p-type WSe_2 and n-type Pb/I co-doped SnSe results in an ultrahigh interface potential, which act as a type of "depletion layer", significantly block the carriers and in turn reduce n and enhance S. Besides, the increased m^* also confirms the strong blocking effect since the carriers with relatively low energy are considerably blocked.

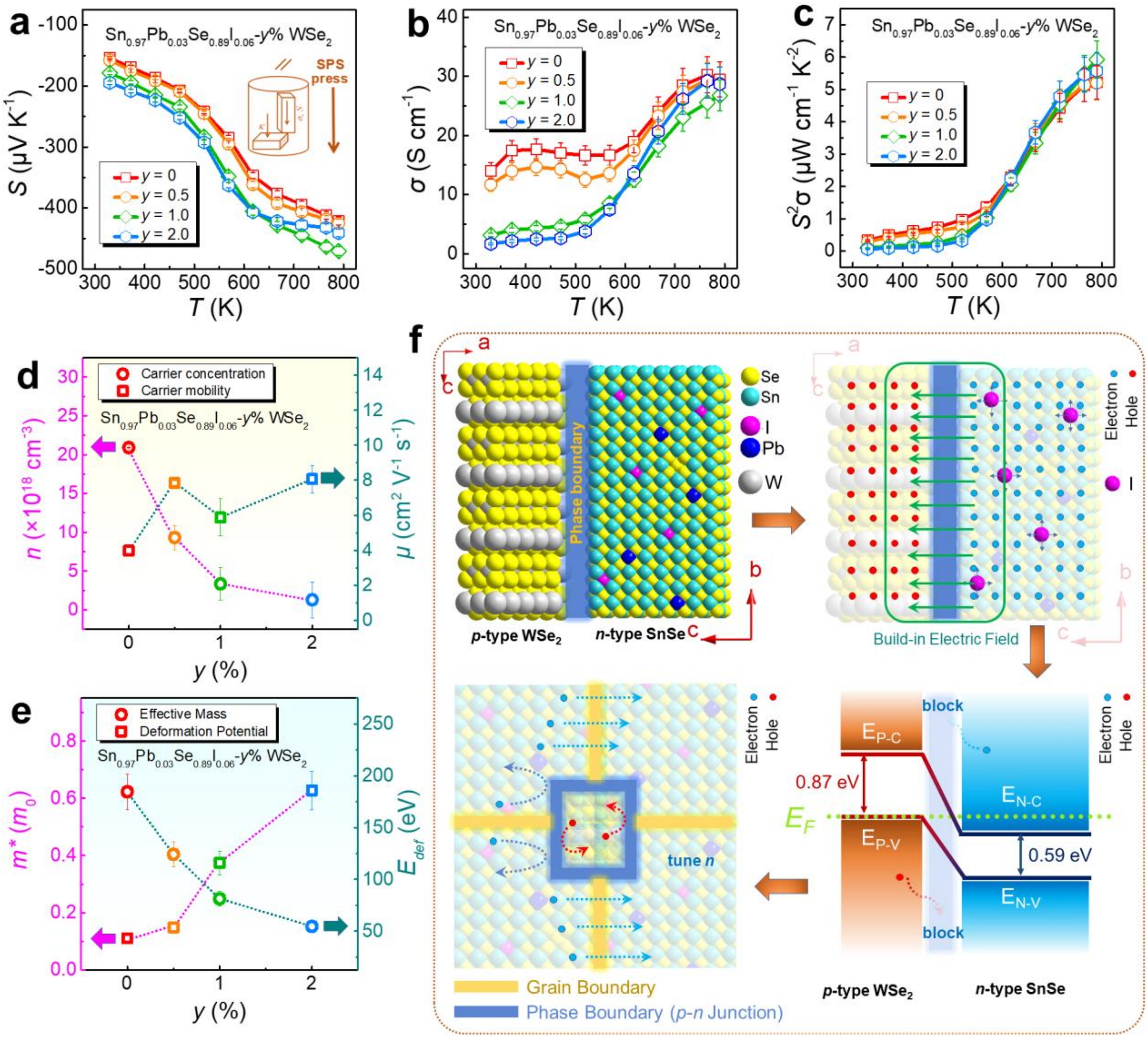

Figure 6. T-dependent (a) S, (b) σ, and (c) $S^2\sigma$ of $Sn_{0.97}Pb_{0.03}Se_{0.89}I_{0.06}$-$y$ % WSe_2. y-dependent room-temperature (d) n and μ, and (e) m^* and E_{def} of $Sn_{0.97}Pb_{0.03}Se_{0.89}I_{0.06}$-$y$ % WSe_2. (f) Illustration of build-in electric field and depletion layer effect at the phase boundaries (p-n junctions) between the p-type WSe_2 and n-type Pb/I co-doped SnSe.

Figure 7(a-b) compare temperature-dependent κ and κ_l of $Sn_{0.97}Pb_{0.03}Se_{0.89}I_{0.06}$-$y$ % WSe_2 measured along the // direction. The calculated temperature-dependent Lorenz number L and κ_e can be referred to **Figure S11**. A low κ of ~0.35 W m^{-1} K^{-1} at 790 K can be seen when $y = 1$, indicating a significant reduction compared with the samples without WSe_2. The reduction of κ_l can be attributed to the introducing of WSe_2 nanoinclusions, since 2D WSe_2 has an ultralow intrinsic κ (only 0.05 W m^{-1} K^{-1}) [41], and these nanoinclusions provide high-density phase boundaries that act as extra phonon scattering sources targeting to scatter the long-wavelength phonons. In addition, these nanoinclusions can also act as phonon scattering centers and cause significant strain fields in the surrounding SnSe lattices, further strengthening the phonon scattering and in turn reducing the κ_l. Callaway model was employed to calrify for the specific frequency range with phonon-scattering centers for mid-to-long-wavelength phonons:

$$\kappa_l = \frac{4\pi\, {k_B}^4\, T^3}{v h^3} \int_0^{\frac{\theta_D}{T}} \frac{z^4 \exp(z)}{\tau_T^{-1}[\exp(z)-1]^2} \mathrm{d}z \tag{1}$$

where k_B is the Boltzmann constant, v is the sound speed, and h is the Planck's constant. In this system, phonon scattering mechanism influences the phonon transport, including impurity/point defect phonon scattering, phonon-phonon Umklapp scattering, phonon scattering by nanoinclusions, and phase boundary phonon scattering. In calculation process, only dominating scattering mechanisms are considered in this work, including the impurity/point defect phonon scattering τ_{im}^{-1} (PD), phonon-phonon Umklapp scattering τ_U^{-1} (U), phase boundary phonon scattering τ_{pb}^{-1} (PB) and electron-phonon scattering τ_{ep}^{-1} (E). Therefore, the total phonon relaxation time can be simplified as:

$$\tau_T^{-1} = \tau_{im}^{-1} + \tau_U^{-1} + \tau_{ep}^{-1} + \tau_{pb}^{-1} \tag{2}$$

or:

$$\tau_T^{-1} = A\omega^4 + \mathrm{B}\omega^2 \mathrm{T} \exp\left(-\frac{\theta_D}{3T}\right) + C\omega^2 + \frac{v}{d} \tag{3}$$

where ω and d are the phonon frequency and the average spatial distance among the WSe_2 nanoinclusions in n-type Pb/I co-doped SnSe matrix. The value of v was measured and θ_D was calculated based on the measured v value (see **Table S3** in the supporting file). The parameters A and B were determined by fitting κ_l data, as listed in **Table S3**. By using the obtained parameters, κ_l for the typical composites of n-type Pb/I co-doped SnSe matrix with p-type 2D-WSe_2 nanoinclusion were calculated through Formula 1 and Formula 2. It can be clearly seen that calculated κ_l is in good agreement with experimental results. It is noted that the obtained average spatial distance d among the nanoinclusions is around 218 nm for the composite sample with y = 1 wt.%, which could be underestimated since we neglected some other scattering mechanisms in the calculations as mentioned above. The parameters used in the calculations for Debye model are given in **Table S3**. It is noted that the obtained average spatial distance d among the nanoinclusions is in good agreement for the composite sample with y = 0.5 and 1.0 wt.%. However, further increase in content y causes to increase the average spatial distance, which could be ascribed to the agglomeration effect of high quantity of content in matrix. **Figure 7(c)** shows 1000/T-dependent κ_l of $Sn_{0.97}Pb_{0.03}Se_{0.89}I_{0.06}$-$y$ % WSe_2. All plots show a linear relationship, indicating that the Umklapp phonon scattering still dominate the phonon scattering after introducing WSe_2 [19, 22, 24, 35].

Figure 7(d) compares determined temperature-dependent ZT of $Sn_{0.97}Pb_{0.03}Se_{0.89}I_{0.06}$-$y$ % WSe_2. A high ZT of ~1.35 at 790 K can be achieved by introducing 1 % WSe_2 nanoinclusions, which ranks as one of the highest values compared to the previously reported works, as shown in **Table 2** and **Figure S12** [35-40, 49-61]. The thermoelectric performance of $Sn_{0.97}Pb_{0.03}Se_{0.89}I_{0.06}$-$y$ % WSe_2 (y = 0 and 1) measured or determined along the ⍰ direction can be seen in **Figure S13** in the supporting information. As can be seen, a peak ZT of ~0.65 can be observed in $Sn_{0.97}Pb_{0.03}Se_{0.89}I_{0.06}$-1 % WSe_2, which is lower than that achieved along the // direction. Furthermore, our results show significantly high repeatability, as confirmed by **Figure S14**.

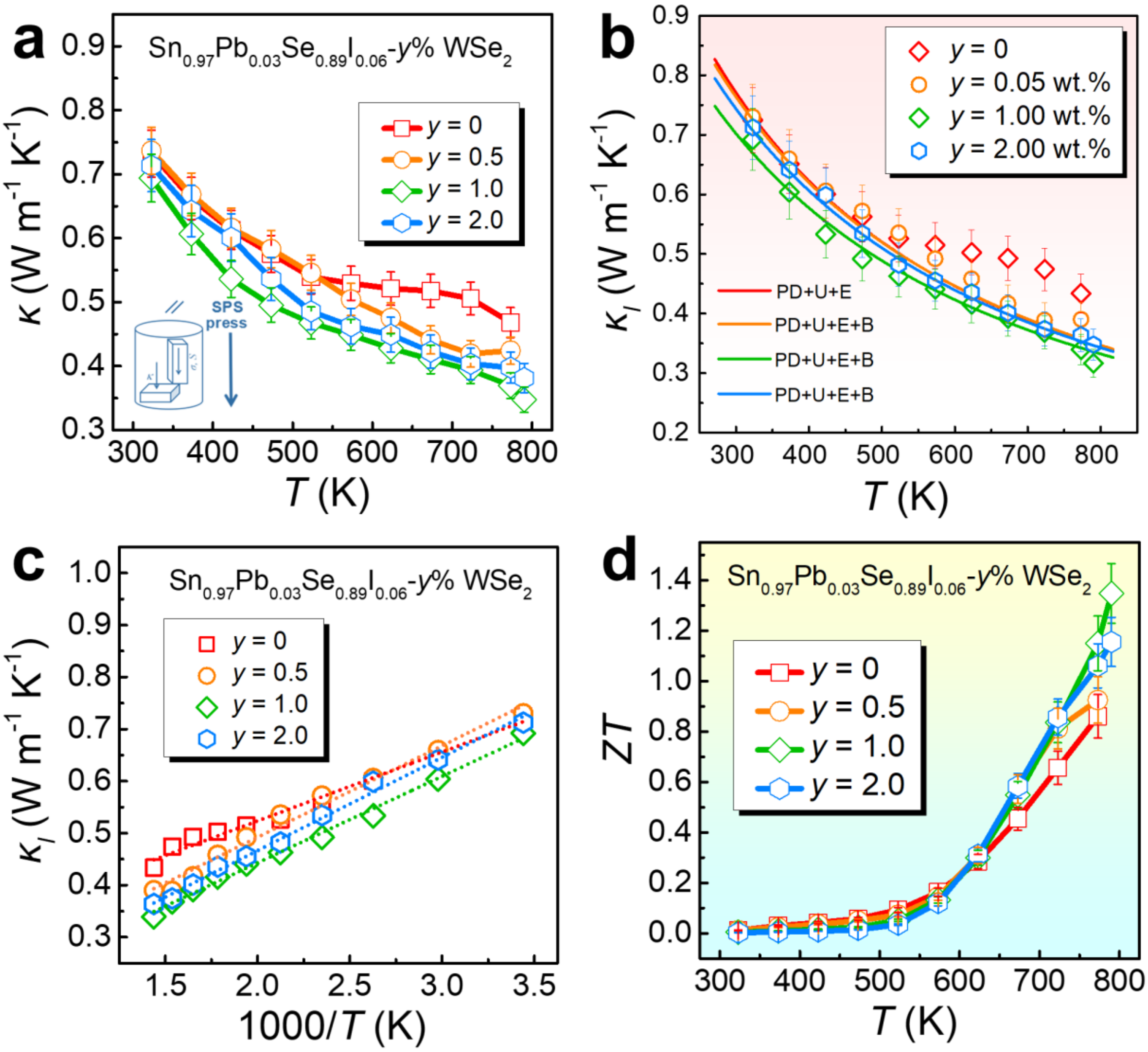

Figure 7. *T*-dependent (a) κ and (b) κ_l of $Sn_{0.97}Pb_{0.03}Se_{0.89}I_{0.06}$-$y$ % WSe_2. The calculated κ_l using Callaway model are included in (b), including impurity/point defect phonon scattering τ_{im}^{-1} (PD), phonon-phonon Umklapp scattering τ_{U}^{-1} (U), phase boundary phonon scattering τ_{pb}^{-1} (PB) and electron-phonon scattering τ_{ep}^{-1} (E). (c) 1000/*T*-dependent κ_l of $Sn_{0.97}Pb_{0.03}Se_{0.89}I_{0.06}$-$y$ % WSe_2. (d) *T*-dependent *ZT* of $Sn_{0.97}Pb_{0.03}Se_{0.89}I_{0.06}$-$y$ % WSe_2. Here y is 0, 0.5, 1.0, and 2.0, respectively. All the properties are measured or determined along the // direction.

Table 2. A summary of n-type polycrystalline bulk SnSe.

Materials	***ZT***	***T*** **(K)**	***σ*** **(S cm^{-1})**	***S*** **(μV K^{-1})**	***S^{2}σ*** **(μW cm^{-1} K^{-2})**	***κ*** **(W m^{-1} K^{-1})**	**Ref.**
$SnSe_{0.87}S_{0.1}I_{0.03}$	~1.0	773	~16	~-500	~4.0	~0.36	[49]
$SnSe_{0.95}$-0.4 % $BiCl_3$	0.7	793	~29	~-414	~5.0	~0.6	[50]
$SnSb_{0.02}Se_{0.96}$	1.1	773	~39	-247	~2.4	~0.17	[35]
$SnSe_{0.95}$-3 % $PbBr_2$	0.54	793	~36	~-360	~4.7	~0.72	[51]
$Sn_{0.97}Re_{0.03}Se_{0.93}Cl_{0.02}$	1.5	798	~30	~-430	~5.8	~0.3	[36]
$Sn_{0.90}Pb_{0.15}Se_{0.95}Cl_{0.05}$	1.2	823	~50	~-360	~6.7	~0.46	[37]
$Sn_{0.90}Pb_{0.10}Se_{0.97}Br_{0.03}$	1.2	773	~35	~-400	~5.6	~0.37	[38]
$Sn_{0.74}Pb_{0.20}Ti_{0.06}Se$	0.4	773	~15	-450	3.0	~0.58	[52]
$SnSe_{0.9}Br_{0.1}$	1.3	773	~28	~-400	~4.5	~0.26	[39]
$Sn_{1.005}Se_{0.94}Br_{0.06}$	1.5	783	~32	~-460	~6.8	~0.36	[40]
Oxygen-isolated $SnSe_{0.97}Br_{0.03}$	1.0	773	~20	~-500	~5.0	~0.36	[53]
$(SnSe)_{0.1}(PbSe)_{0.9}$	1.0	773	~490	~-180	~16.5	~1.20	[54]
$Sn_{0.97}Bi_{0.03}Se$	-	723	~3.0	~-390	~0.45	-	[55]
$Sn_{0.94}Bi_{0.06}Se$	0.025	723	~5.5	~-190	~0.2	~0.53	[56]
$SnSe_{0.9375}Te_{0.0625}$	-	673	~3.6	~-280	~0.3	-	[57]
$SnSe_{0.98}$	~0.07	773	~3.0	~-380	~0.4	~0.5	[58]
$Sn_{0.8}Sb_{0.2}Se$	0.3	908	~100	~-125	~1.0	~0.46	[59]
SnSe + SiC	0.125	300	~7.3	-581	~2.5	~0.6	[60]
$SnSe_{0.94}Cl_{0.06}$ + $SnSe_2$	0.56	773	~32	~-300	~2.9	~0.43	[61]
$Sn_{0.97}Pb_{0.03}Se_{0.89}I_{0.06}$-$y$ % WSe_2, **This work**	1.35	790	26.6	-470.7	5.9	0.35	

4. Conclusion

In this work, a high *ZT* of ~1.35 at 790 K has been realized in n-type polycrystalline SnSe by a combination of Pb/I co-doping and introducing 2D WSe_2 nanoinclusions to form WSe_2/SnSe p-n junctions. Calculation results confirm the I-doping shifts the Fermi level up into the conduction bands, making the system n-type. A high $S^2\sigma$ of ~5.9 μW cm^{-1} K^{-2} is achieved by tuning a n of 3.34×10^{18} cm^{-3} through 3 % I-doping and carrier blocking by introducing WSe_2/SnSe p-n junctions (1 % WSe_2). Meanwhile, a low κ of ~0.35 W m^{-1} K^{-1} is obtained, benefited from the strengthened phonon scattering at Pb and I that act as point defects, as well as the high-density phase boundaries by introducing WSe_2 nanoinclusions. This study indicates that rational band engineering and nanostructural design possess great potential for securing high thermoelectric performance in n-type polycrystalline SnSe.

Author contributions

Y.X.C., X.L.S., Z.H.Z., P.F. and Z.G.C. designed the experiments; Y.X.C., X.L.S., F.L., W.D.L. and W.Y.C. performed the material synthesis and sample measurement; X.R.L., G.X.L. and J.T.L. performed the theoretical calculation; Y.X.C., X.L.S. and Z.H.Z. conducted the SEM and TEM characterization. Everyone was involved in writing the article.

Conflicts of interest

The authors declare no competing financial interest.

Declaration of competing interest

The authors declare that they have no known competing financial interests or personal relationships that could have appeared to influence the work reported in this paper.

Acknowledgements

This work was financially supported by the National Natural Science Foundation of China (Grant No. 11604212), Guangdong Basic and Applied Basic Research Foundation (Grant No. 2019A1515110107 and 2020A1515010515), Shenzhen Key Lab Fund (ZDSYS 20170228105421966), Australia Research Council, Innovation Centre for Sustainable Steel Project, and USQ Strategic research fund. The authors also are thankful for the assistance on HAADF-STEM observation received from the Electron Microscope Center of the Shenzhen University.

Reference

[1] X. Shi and L. Chen, Nat. Mater. 15 (2016) 691-692.

[2] X.-L. Shi, J. Zou, and Z.-G. Chen, Chem. Rev. 120 (2020) 7399-7515.

[3] Z.-G. Chen, X. Shi, L.-D. Zhao, and J. Zou, Prog. Mater. Sci. 97 (2018) 283-346.

[4] G. Tan, L.D. Zhao, and M.G. Kanatzidis, Chem. Rev. 116 (2016) 12123-12149.

[5] X.-L. Shi, H. Wu, Q. Liu, W. Zhou, S. Lu, Z. Shao, M. Dargusch, and Z.-G. Chen, Nano Energy 78 (2020) 105195.

[6] M. Hong, Z.G. Chen, L. Yang, Z.M. Liao, Y.C. Zou, Y.H. Chen, S. Matsumura, and J. Zou, Adv. Energy Mater. 8 (2017) 1702333.

[7] Y. Wu, Z. Chen, P. Nan, F. Xiong, S. Lin, X. Zhang, Y. Chen, L. Chen, B. Ge, and Y. Pei, Joule 3 (2019) 1276-1288.

[8] J. Li, X. Zhang, Z. Chen, S. Lin, W. Li, J. Shen, I.T. Witting, A. Faghaninia, Y. Chen, and A. Jain, Joule 2 (2018) 976-987.

[9] B. Zhong, Y. Zhang, W. Li, Z. Chen, J. Cui, W. Li, Y. Xie, Q. Hao, and Q. He, Appl. Phys. Lett. 105 (2014) 123902.

[10] W. Liu, L. Yang, Z.-G. Chen, and J. Zou, Adv. Mater. 32 (2020) 1905703.

[11] C. Chang, M. Wu, D. He, Y. Pei, C.-F. Wu, X. Wu, H. Yu, F. Zhu, K. Wang, and Y. Chen, Science 360 (2018) 778-783.

[12] L.-D. Zhao, C. Chang, G. Tan, and M.G. Kanatzidis, Energy Environ. Sci. 9 (2016) 3044-3060.

[13] C. Chang, G. Tan, J. He, M.G. Kanatzidis, and L.-D. Zhao, Chem. Mater. 30 (2018) 7355-7367.

[14] M. Jin, X.-L. Shi, T. Feng, W. Liu, H. Feng, S.T. Pantelides, J. Jiang, Y. Chen, Y. Du, J. Zou, and Z.-G. Chen, ACS Appl. Mater. Interfaces 11 (2019) 8051-8059.

[15] Y. Zheng, X.-L. Shi, H. Yuan, S. Lu, X. Qu, W. Liu, L. Wang, K. Zheng, J. Zou, and Z.-G. Chen, Mater. Today Phys. 13 (2020) 100198.

[16] L.-D. Zhao, G. Tan, S. Hao, J. He, Y. Pei, H. Chi, H. Wang, S. Gong, H. Xu, and V.P. Dravid, Science 351 (2016) 141-144.

[17] S. Sassi, C. Candolfi, J.B. Vaney, V. Ohorodniichuk, P. Masschelein, A. Dauscher, and B. Lenoir, Appl. Phys. Lett. 104 (2014) 212105.

[18] X.-L. Shi, W.-Y. Chen, X. Tao, J. Zou, and Z.-G. Chen, Mater. Horiz. (2020). DOI: 10.1039/D0MH00954G.

[19] X. Shi, Z.-G. Chen, W. Liu, L. Yang, M. Hong, R. Moshwan, L. Huang, and J. Zou, Energy Storage Mater. 10 (2018) 130-138.

[20] M. Dargusch, X.-L. Shi, X.Q. Tran, T. Feng, F. Somidin, X. Tan, W. Liu, K. Jack, J. Venezuela, H. Maeno, T. Toriyama, S. Matsumura, S.T. Pantelides, and Z.-G. Chen, J. Phys. Chem. Lett. 10 (2019) 6512-6517.

[21] X.-L. Shi, W.-D. Liu, A.-Y. Wu, V.T. Nguyen, H. Gao, Q. Sun, R. Moshwan, J. Zou, and Z.-G. Chen, InfoMat 2 (2020) 1201-1215.

[22] X.L. Shi, K. Zheng, M. Hong, W.D. Liu, R. Moshwan, Y. Wang, X.-L. Qu, Z.G. Chen, and J. Zou, Chem. Sci. 9 (2018) 7376-7389.

[23] Y.-X. Chen, Z.-H. Ge, M. Yin, D. Feng, X.-Q. Huang, W. Zhao, and J. He, Adv. Funct. Mater. 26 (2016) 6836-6845.

[24] X. Shi, A. Wu, T. Feng, K. Zheng, W. Liu, Q. Sun, M. Hong, S.T. Pantelides, Z.G. Chen, and J. Zou, Adv. Energy Mater. 9 (2019) 1803242.

[25] J.C. Li, D. Li, X.Y. Qin, and J. Zhang, Scripta Mater. 126 (2017) 6-10.

[26] Y.-M. Han, J. Zhao, M. Zhou, X.-X. Jiang, H.-Q. Leng, and L.-F. Li, J. Mater. Chem. A 3 (2015) 4555-4559.

[27] Y. Zhu, J. Carrete, Q.-L. Meng, Z. Huang, N. Mingo, P. Jiang, and X. Bao, J. Mater. Chem. A 6 (2018) 7959-7966.

[28] D. Li, J. Li, X. Qin, J. Zhang, H. Xin, C. Song, and L. Wang, Energy 116 (2016) 861-866.

[29] Y. Li, F. Li, J. Dong, Z. Ge, F. Kang, J. He, H. Du, B. Li, and J.-F. Li, J. Mater. Chem. C 4 (2016) 2047-2055.

[30] S.R. Popuri, M. Pollet, R. Decourt, F.D. Morrison, N.S. Bennett, and J.W.G. Bos, J. Mater. Chem. C 4 (2016) 1685-1691.

[31] X. Shi, A. Wu, W. Liu, R. Moshwan, Y. Wang, Z.-G. Chen, and J. Zou, ACS Nano 12 (2018) 11417-11425.

[32] H. Ju, M. Kim, D. Park, and J. Kim, Chem. Mater. 29 (2017) 3228-3236.

[33] Y.K. Lee, Z. Luo, S.P. Cho, M.G. Kanatzidis, and I. Chung, Joule 3 (2019) 719-731.

[34] X.-L. Shi, X. Tao, J. Zou, and Z.-G. Chen, Adv. Sci. 7 (2020) 1902923.

[35] X.L. Shi, K. Zheng, W.D. Liu, Y. Wang, Y.Z. Yang, Z.G. Chen, and J. Zou, Adv. Energy Mater. 8 (2018) 1800775.

[36] Z.H. Ge, Y. Qiu, Y.X. Chen, X. Chong, J. Feng, Z.K. Liu, and J. He, Adv. Funct. Mater. 29 (2019) 1902893.

[37] J. Cha, C. Zhou, Y.K. Lee, S.-P. Cho, and I. Chung, ACS Appl. Mater. Interfaces 11 (2019) 21645-21654.

[38] C. Chang, Q. Tan, Y. Pei, Y. Xiao, X. Zhang, Y.-X. Chen, L. Zheng, S. Gong, J.-F. Li, and J. He, RSC Adv. 6 (2016) 98216-98220.

[39] S. Li, Y. Wang, C. Chen, X. Li, W. Xue, X. Wang, Z. Zhang, F. Cao, J. Sui, and X. Liu, Adv. Sci. 5 (2018) 1800598.

[40] P.-P. Shang, J. Dong, J. Pei, F.-H. Sun, Y. Pan, H. Tang, B.-P. Zhang, L.-D. Zhao, and J.-F. Li, Research 2019 (2019) 1-10.

[41] C. Chiritescu, D.G. Cahill, N. Nguyen, D. Johnson, A. Bodapati, P. Keblinski, and P. Zschack, Science 315 (2007) 351.

[42] Q. Cheng, J. Pang, D. Sun, J. Wang, S. Zhang, F. Liu, Y. Chen, R. Yang, N. Liang, X. Lu, Y. Ji, J. Wang, C. Zhang, Y. Sang, H. Liu, and W. Zhou, InfoMat 2 (2020) 656-697.

[43] S. Yang, Y. Liu, M. Wu, L.-D. Zhao, Z. Lin, H.-c. Cheng, Y. Wang, C. Jiang, S.-H. Wei, L. Huang, Y. Huang, and X. Duan, Nano Res. 11 (2018) 554-564.

[44] J. Hong and O. Delaire, Mater. Today Phys. 10 (2019) 100093.

[45] G. Kresse and D. Joubert, Phys. Rev. B 59 (1999) 1758.

[46] J.P. Perdew, K. Burke, and M. Ernzerhof, Phys. Rev. Lett. 77 (1996) 3865.

[47] J.P. Perdew, J.A. Chevary, S.H. Vosko, K.A. Jackson, M.R. Pederson, D.J. Singh, and C. Fiolhais, Phys. Rev. B 46 (1992) 6671.

[48] H.J. Monkhorst and J.D. Pack, Phys. Rev. B 13 (1976) 5188.

[49] Q. Zhang, E.K. Chere, J. Sun, F. Cao, K. Dahal, S. Chen, G. Chen, and Z. Ren, Adv. Energy Mater. 5 (2015) 1500360.

[50] X. Wang, J. Xu, G. Liu, Y. Fu, Z. Liu, X. Tan, H. Shao, H. Jiang, T. Tan, and J. Jiang, Appl. Phys. Lett. 108 (2016) 083902.

[51] D. Li, X. Tan, J. Xu, G. Liu, M. Jin, H. Shao, H. Huang, J. Zhang, and J. Jiang, RSC Adv. 7 (2017) 17906-17912.

[52] F. Li, W. Wang, X. Qiu, Z.-h. Zheng, P. Fan, J.-t. Luo, and B. Li, Inorg. Chem. Front. 4 (2017) 1721-1729.

[53] M. Zhang, D. Wang, C. Chang, T. Lin, K. Wang, and L.-D. Zhao, J. Mater. Chem. C 7 (2019) 10507-10513.

[54] C.F. Wu, T.R. Wei, and J.F. Li, Phys. Chem. Chem. Phys. 17 (2015) 13006-13012.

[55] X. Li, C. Chen, W. Xue, S. Li, F. Cao, Y. Chen, J. He, J. Sui, X. Liu, and Y. Wang, Inorg. Chem. 57 (2018) 13800-13808.

[56] V.Q. Nguyen, T.H. Nguyen, J.E. Lee, S.-D. Park, J.Y. Song, H.-M. Park, A.T. Duong, and S. Cho, Nanoscale Res. Lett. 13 (2018) 200.

[57] S. Chen, K. Cai, and W. Zhao, Physica. B 407 (2012) 4154-4159.

[58] Q. Li, L. Zhang, J. Yin, Z. Sheng, X. Chu, F. Wang, and F. Zhu, J. Alloys Compd. 745 (2018) 513-518.

[59] J. Gainza, F. Serrano-Sánchez, M. Gharsallah, F. Carrascoso, J. Bermúdez, O.J. Dura, F.J. Mompean, N. Biskup, J.J. Meléndez, J.L. Martínez, J.A. Alonso, and N.M. Nemes, J. Appl. Phys. 126 (2019) 045105.

[60] H. Ju and J. Kim, Ceram. Int. 42 (2016) 9550-9556.

[61] Y. Shu, X. Su, H. Xie, G. Zheng, W. Liu, Y. Yan, T. Luo, X. Yang, D. Yang, and C. Uher, ACS Appl. Mater. Interfaces 10 (2018) 15793-15802.

Declaration of interests

☒ The authors declare that they have no known competing financial interests or personal relationships that could have appeared to influence the work reported in this paper.

☐The authors declare the following financial interests/personal relationships which may be considered as potential competing interests:

CRediT author statement

Yue-Xing Chen: Conceptualization, Methodology, Validation, Formal analysis, Investigation, Data Curation, Writing - Original Draft;

Xiao-Lei Shi: Conceptualization, Methodology, Formal analysis, Investigation, Data Curation, Writing - Original Draft, Visualization;

Zhuang-Hao Zheng: Conceptualization, Formal analysis, Resources, Data Curation, Writing - Review & Editing, Supervision, Project administration;

Fu Li: Conceptualization, Formal analysis, Resources;

Wei-Di Liu: Formal analysis;

Wen-Yi Chen: Formal analysis;

Xin-Ru Li: Software;

Guang-Xing Liang: Software;

Jing-Ting Luo: Software, Resources;

Ping Fan: Resources, Supervision, Project administration, Funding acquisition;

Zhi-Gang Chen: Conceptualization, Formal analysis, Writing - Review & Editing, Supervision, Project administration, Funding acquisition.